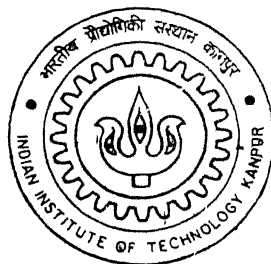


# **AERODYNAMIC CHARACTERISTICS OF A 75° DELTA WING**

**By**

**Behara Suresh**



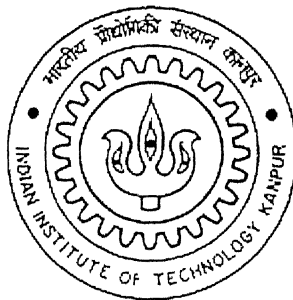
**DEPARTMENT OF AEROSPACE ENGINEERING**

**Indian Institute of Technology Kanpur**

**MARCH, 2002**

# AERODYNAMIC CHARACTERISTICS OF A $75^0$ DELTA WING

By  
**BEHARA SURESH**



DEPARTMENT OF AEROSPACE ENGINEERING  
INDIAN INSTITUTE OF TECHNOLOGY, KANPUR

# AERODYNAMIC CHARACTERISTICS OF A $75^0$ DELTA WING

*A Thesis* Submitted  
in Partial Fulfillment of the Requirements  
for the Degree of Master of Technology

By  
**BEHARA SURESH**

DEPARTMENT OF AEROSPACE ENGINEERING  
INDIAN INSTITUTE OF TECHNOLOGY, KANPUR  
February 2002

1 3 FEB 2003 / A2

पुरुषोत्तम काशीनाथ केकर पुस्तकालय

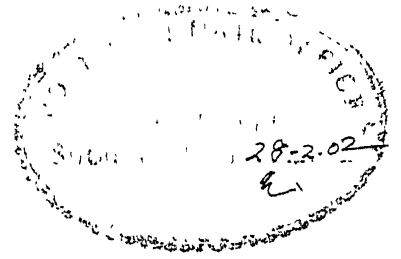
भारतीय औद्योगिकी संस्थान कानपुर

अवधि क्र० A-141805



A141805

# CERTIFICATE



It is certified that the work contained in this thesis entitled "*AERODYNAMIC CHARACTERISTICS OF 75deg DELTA WING*", by Behara Suresh, has been carried out under my supervision and that this work has not been submitted elsewhere for any degree.

A handwritten signature in black ink, appearing to read "K Poddar", written over a horizontal line.

Dr. Kamal Poddar

Department of Aerospace Engineering  
Indian Institute of Technology, Kanpur

# ACKNOWLEDGEMENT

I feel great pleasure in expressing deep sense of gratitude and sincere thanks to my thesis supervisors Dr KAMAL PODDAR for his discerning guidance, invaluable suggestions and constant encouragement throughout the course of thesis work. I have learnt a lot from him, which would be of great help in future. Working with him, has been the most exciting phase of my career.

I am highly thankful to Mr. Brajesh chandra, Dr Rajeev Gupta and Mr. Chaturi Singh without whose help I could not have finished my thesis successfully. I appreciate and extend my thanks to Mr. Sarad Saxena and staff of NWTF for their kindly help in erection of my experimental set up.

Helping hands of staff in the low speed aerodynamics lab and the aero workshop are greatly acknowledged.

Indian Institute of Technology, Kanpur.

Behara Suresh

February 2002

Dedicated to  
my loving parents

# ABSTRACT

In the present study, the effect of leading edge vortices on the aerodynamic forces and moments is experimentally investigated. Experiments were conducted at the National Wind Tunnel Facility, IIT Kanpur. A delta wing model having  $75^\circ$  sweep angle was tested to find factors influencing the aerodynamic characteristics. A six-component strain gage balance was used to measure the forces and moments acting on the model. Investigation was carried out at constant wind speed (30m/s). The angle of attack was varied from  $-10^\circ$  to  $61^\circ$  in steps of  $2^\circ$ , and the sideslip angles were taken to be  $-10.75^\circ$ ,  $-5.75^\circ$ ,  $0^\circ$ ,  $4.6^\circ$  and  $10.12^\circ$ . Results were presented on the wind axes at the C.G. of the model. Smoke flow visualization and laser sheet technique were used to observe the cross-sectional views of the leading-edge vortices, their break down, the effect of angle of attack on the vortices and the location of breakdown which influenced the forces and moments on the model.

At  $35^\circ$  angle of attack with  $0^\circ$  sideslip lift coefficient drops suddenly. Lift and drag coefficients have a tendency to decrease with sideslip angle ( $\beta$ ). Yaw force coefficient ( $C_Y$ ) and yawing moment coefficient ( $C_{m_y}$ ) are positive for positive sideslip angles at lower values of  $\alpha$  but they are always negative for both positive and negative sideslip angles at higher angles of attack. This is possible as the flow is unsteady at high  $\alpha$ . Their variation is symmetric with  $\beta$ . On the other hand, the pitching moment coefficient  $C_{m_p}$  does not have significant variation with  $\beta$ , while the rolling moment coefficient is sensitive to both  $\alpha$  &  $\beta$ .



# Contents

<b>List of Figures</b>	<b>i</b>
<b>Nomenclature</b>	<b>iii</b>
<b>1 INTRODUCTION</b>	<b>1</b>
1.1 Literature survey	2
1.2 Present study	6
<b>2 EXPERIMENTAL ARRANGEMENT</b>	<b>7</b>
2.1 Experimental Facility	7
2.2 Model Description	8
2.3 Instrumentation	8
2.4 Force Measurement	10
<b>3 DATA ACQUISITION AND ANALYSIS</b>	<b>14</b>
3.1 LabVIEW	14
3.2 Data Acquisition	15
3.3 Data Analysis	15
<b>4 RESULTS AND DISCUSSION</b>	<b>18</b>
4.1 Effect of Angle of Attack ( $\alpha$ )	18
4.2 Effect of Sideslip Angle ( $\beta$ )	20
4.3 Flow Visualization Results	20
<b>5 CONCLUSTION AND SCOPE FOR FUTURE WORK</b>	<b>22</b>
5.1 Conclusions	22
5.2 Scope for Future Work	23

<b>References</b>	<b>24</b>
<b>Figures</b>	<b>26</b>
<b>Appendix-A</b>	<b>54</b>

# List of Figures

- Figure 1 Aerodynamic layout of Wind Tunnel
- Figure 2 Body Axis and Wind Axis systems
- Figure 3 Model geometry
- Figure 4 Experimental setup
- Figure 5 Flow field over the wing surface at positive angles of attack
- Figure 6 Visualization of vortices
- Figure 7 Front panel of the data acquisition program
- Figure 8 Block diagram of typical analysis routine
- Figure 9 Variation of all forces and moments with the angle of attack at zero sideslip angle
- Figure 10 Variation of all aerodynamic coefficients with the angle of attack at zero sideslip angle
- Figure 11 Variation of drag coefficient with lift coefficient at zero sideslip angle
- Figure 12 Variation of pitching moment coefficient with lift coefficient at zero sideslip angle
- Figure 13 Variation of yaw coefficient with the angle of attack at zero sideslip angle
- Figure 14 Variation of pitching moment coefficient with the angle of attack at zero sideslip angle
- Figure 15 Variation of yawing moment coefficient with the angle of attack at zero sideslip angle
- Figure 16 Variation of rolling moment coefficient with angle of attack at zero sideslip angle
- Figure 17 Variation of aerodynamic forces and moments with angle of attack at  $4.6^{\circ}$  sideslip angle.
- Figure 18 Variation of aerodynamic forces and moments with angle of attack at  $-5.75^{\circ}$  sideslip angle.
- Figure 19 Variation of aerodynamic forces and moments with angle of attack at  $10.12^{\circ}$  sideslip angle.
- Figure 20 Variation of aerodynamic forces and moments with angle of attack at  $-10.75^{\circ}$  sideslip angle.

- Figure 21 Effect of sideslip angle on lift coefficient
- Figure 22 Effect of sideslip angle on drag coefficient
- Figure 23 Effect of sideslip angle on yaw force coefficient
- Figure 24 Effect of sideslip angle on pitching moment coefficient
- Figure 25 Effect of sideslip angle on yawing moment coefficient
- Figure 26 Effect of sideslip angle on rolling moment coefficient
- Figure 27 Variation of drag coefficient with lift coefficient, sideslip angle is parameter
- Figure 28 Variation of pitching moment coefficient with lift coefficient, sideslip angle is parameter

# NOMENCLATURE

$A_x$	Axial force on the balance
$N_1, N_2$	Normal force components on the balance
$S_1, S_2$	Side force components on the balance
$R_m$	Rolling moment on the balance
$A_{x_{bal}}$	Axial force at the balance center
$N_{bal}$	Normal force at the balance center
$S_{bal}$	Side force at the balance center
$M_{p_{bal}}$	Pitching moment at the balance center
$M_{y_{bal}}$	Yawing moment at the balance center
$M_{r_{bal}}$	Rolling moment at the balance center
$A_{x_b}$	Axial force on the body axis
$N_{F_b}$	Normal force on the body axis
$S_{F_b}$	Side force on the body axis
$M_{p_b}$	Pitching moment on the body axis
$M_{y_b}$	Yawing moment on the body axis
$M_{r_b}$	Rolling moment on the body axis
$D_w$	Drag force on the wind axis
$L_w$	Lift force on the wind axis
$Y_w$	Yaw force on the wind axis
$M_{p_w}$	Pitching moment on the wind axis
$M_{y_w}$	Yawing moment on the wind axis

$M_{r_w}$	Rolling moment on the wind axis
$C_L$	Lift force coefficient in the wind axis system
$C_D$	Drag force coefficient in the wind axis system
$C_Y$	Yaw force coefficient in the wind axis system
$C_{m_p}$	Pitching moment coefficient in the wind axis system
$C_{m_y}$	Yawing moment coefficient in the wind axis system
$C_{m_r}$	Rolling moment coefficient in the wind axis system
$U_\infty$	Free stream velocity
$\alpha$	Angle of attack
$\beta$	Side slip angle
$\psi$	Yaw angle
$\rho$	Free stream density

# INTRODUCTION

In modern air combat tactics, maneuverability of a fighter aircraft plays an important role. During close-contact air fighting, the pilot has to perform sharp turning and rapid climbing for attacking or escaping. So the high performance of the aircraft needs to be maintained by having high lift and refraining from wing stall at high angles of attack flight. This can be achieved by using highly swept, slender, low aspect ratio wings. Delta wing has these characteristics and is thus, favorably used in the jet fighters.

The flow over the delta wing is vortex<sup>1</sup> dominated flow. At subsonic speeds, the flow separates at the leading edge of the wing. This separated shear layer rolls into a large vortex over the leeward side of the wing. Very large axial flow component is present in these two leading edge vortices. This high flow velocity in the core of the vortex is the region of low pressure and this low pressure generates suction or lift. This is also known as vortex lift. Flow visualization on delta wings has also revealed that the lift produced on the delta wing is augmented by the two coherent leading edge vortices formed on its upper surface. Stall on the delta wing occurs at a large angle of attack, which leads to vortex breakdown. Vortex breakdown causes the destruction of the tight and coherent vortex. The core becomes highly turbulent, the diameter of the core increases, and the high axial velocity in the core ceases to exist. This phenomenon causes the wing to lose lift.

In spite of all the benefits from highly swept delta shaped wing for the jet fighter, this vortex breakdown is the major cause for deteriorating flight performance. Sometimes the breakdown occurs over one of the wings only causing problems in controlling the flight. The force imbalance between the two wings causes high rolling moment. Once the angle of attack is large enough for the vortex breakdown to have crossed the trailing edge and move upstream, the wing experiences a substantial change in the local pressure field, producing a decrease in lift curve slope and an increase in the positive pitching moment. At sufficiently high angles of attack, breakdown of the entire vortex flow field occurs so

that separation without concentrated vortex feature exists over the wing. The location of the vortex breakdown moves upstream as the angle of attack is further increased. At higher angles of attack, vortex breakdown occurs closer to the wing apex and the flow may breakup into unsteady turbulent wake.

## ***1.1 Literature survey***

Delta wings are used in fighter aircraft, which can fly at supersonic speeds. Delta or triangular wings were first tested by Winter in 1935. Because of the ability of delta wing planform to satisfy the various requirements of stable and controllable flight at high angle of attack, a considerable number of studies have been undertaken to elucidate their flow characteristics. But the vehicles spend most of the time at subsonic speeds in combat and moreover, they fly at low speeds for take off and landing. So, great importance is attached to study the aerodynamic characteristics of the delta wing and the flow mechanism over the wing. For delta wing with sharp leading edges, enforcement of the Kutta condition at the leading edge ensures that the flow separates forming leading-edge vortices. These structures are fed from the vorticity, which is generated by the merging of the upper and lower surface leading edge boundary layers.

Delta wings are not without limitations. Low lift is generated on delta wings because of their low Aspect Ratio (AR), requiring high angle of attack (with consequent high drag) for take off and landing. If the delta wing is sharp-edged or the flow has separated, lift is augmented over the wing upper surface, which induces high velocities on the wing upper surface, thereby reducing the surface pressure. This vortex lift, as shown by Polhamus<sup>2</sup>, is equal to the leading-edge suction that could have been developed if the flow on the wing was fully attached. Thus, the net effect of enforcing leading-edge flow separation on a flat delta wing is to cause effective rotation of the leading-edge suction force to the plane of the normal force. This causes a substantial increase in drag as the leading-edge suction is lost. As shown by Lamar<sup>3</sup>, theoretically and experimentally, the substantial lift increases due to the leading-edge vortices and are augmented through entrainment



resulting from the core pressure deficit. Some attempts were made to increase the lift on the delta wing with spanwise blowing. Seginar & Salomen<sup>4</sup> investigated 60° delta wing by experimentally blowing the wind spanwise over wing surface at angles of attack up to 60° and yaw angles up to 36°. They found significant improvement in lift curve slope and maximum lift.

Ericsson and Redding<sup>5</sup> performed an analytical approach to analyze the steady and unsteady aerodynamics of sharp-edged slender wings. The results showed that the slender wing theory could be modified to give static and dynamic characteristics of the potential incompressible flow. A semi-empirical approximation was developed for the vortex induced loads, and it was shown that the analytic approximation for sharp-edged slender wings matched with experimentally determined steady and unsteady aerodynamics.

Self-induced roll oscillations are major limitations on low speed maneuvers of aircraft utilizing delta wings. Nguyen et al<sup>6</sup> made an effort to gain experimental insight into the self-induced wing rock phenomenon. They successfully recorded roll angle oscillations during self-induced wing rock of a flat plate delta wing with 80° leading edge sweep, and then calculated the resulting rolling moments. They obtained the limiting angle of attack at which wing rock occurred. In continuation of this work, Levin<sup>7</sup> tested two free-to-roll delta wings having leading edge sweeps of 76° and 80°, but observed that only the wing with 80° sweep underwent periodic self-induced roll oscillations. A considerable drop in the average normal force of the free-to-roll wing was found relative to the normal force obtained in the static tests. On the other hand Ericsson<sup>8</sup> studied the wing rock of the delta wing using analytical approach. He inferred that the cause of the wing rock was asymmetric vortex shedding from the wing leading edges and not by vortex burst. The breakdown of the leading edge vortices of a delta wing could lead to static instability with associated roll divergence. He compared his results with the experimental data and described that the lift-off of one of the leading edge vortices would cause a loss of lift, which resulted in wing rock. Terry, Malcom and Lewis<sup>9</sup> investigated the phenomenon of wing rock on delta wing models with 70°, 75°, 80° and 85° sweeps in a free-to-roll configuration and forced oscillation configuration. They observed that wing rock

occurred in the absence of vortex breakdown, static hysteresis, and even asymmetric liftoff. Finally, they concluded that these phenomena were, therefore, not the necessary conditions of wing rock. The presence of these phenomena, however, can have strong influence on characteristics such as amplitude and frequency of wing rock.

Wentz Jr.<sup>10</sup> conducted systematic wind-tunnel investigations of vortex breakdown on sharp edged delta wings with sweep angles from  $45^{\circ}$  to  $85^{\circ}$  at Reynolds numbers of about  $1 \times 10^6$  with flow visualization. He observed that the angle at which breakdown occurred increased with the sweep for sweep angles less than  $75^{\circ}$ . For all sweep angles greater than  $75^{\circ}$ , breakdown occurred at a constant angle of attack and the breakdown on these wings are quite sensitive to yaw. Whereas Payne, Ng and Nelson<sup>11</sup> performed smoke flow visualization on a series of flat plate delta wings having sweep angles of  $70^{\circ}$ ,  $75^{\circ}$ ,  $80^{\circ}$  and  $85^{\circ}$  in an effort to understand the dynamics of the vortex breakdown on delta wings at high angles of attack. They tested the models at different speeds. At low speeds (up to 3m/s) it was observed that there was a tendency of the location of vortex breakdown to move to and fro on the more highly swept wings. For  $70^{\circ}$  wing, the breakdown locations of the vortices were approximately symmetric in mean breakdown location for the wings of  $80^{\circ}$  and  $85^{\circ}$  sweeps at both low (3m/s) and relatively high (15 m/s) speeds.

Roos and Kegelman<sup>12</sup> investigated the influence of sweep angle on delta wing flows and concluded that vortex core trajectories, vortex burst locations and wing lift show no significant sensitivity to Reynolds Number (Re) changes at higher Re,  $0.34 \times 10^6$  to  $2 \times 10^6$ . Whereas, Lee et al<sup>14</sup> suggested that for sharp edged wings the vortex breakdown location is independent of Re. They conducted the experiments at Re between  $3 \times 10^4$  to  $6 \times 10^4$  and also inferred that aerodynamic forces on delta wings are insensitive to Re. On the other hand experiments were undertaken by Lance and Brian<sup>15</sup> to determine the aerodynamic characteristics of  $60^{\circ}$  and  $70^{\circ}$  delta wings at low Re. A change of characteristics of the vortical flow-field appears when Re is decreased from  $4 \times 10^4$  to  $2 \times 10^4$ . At  $Re = 2 \times 10^4$  for  $60^{\circ}$  delta wing vortex breakdown is delayed at given angle of attack. Also, it is shown that there is no significant effect of Re on the lift.

Interestingly, Zvi<sup>16</sup> concentrated on the effect of the test section walls on the dynamics of the vortex breakdown. In his investigation of the influence of the test section walls on the location of the vortex breakdown, he tested a flat delta wing. Presence of the walls induced up-wash on the wing surface. This up-wash is relatively small near the apex of the wing and larger on the trailing edge.

To understand the phenomenon of vortex breakdown and its effect on aerodynamic characteristics of delta wings with large sweep angle at high angles of attack, Dr. Kamal Poddar initiated research work in Low Speed Aerodynamics Laboratory, IIT Kanpur. Some graduate students participated in this research program for their thesis.

Singh<sup>17</sup> performed smoke flow visualization and surface static pressure measurements over a delta wing. It was shown that for angles of attack beyond  $27^\circ$ , bubble type, asymmetric vortex breakdown occurred. At fixed angle of attack the breakdown location oscillated a mean position and moved upstream with increased angle of attack. Sinha<sup>18</sup> tested  $70^\circ$  delta wing and succeeded in moderating the vortex breakdown providing suction at the vortex core. He placed a probe at the trailing edge and created suction to reduce the oscillations of the wing. Chattopadhyay<sup>19</sup> investigated flow over  $80^\circ$  delta wing having moderate to high amplitude of roll oscillations. He found a linear positive relation of the frequency of oscillation with Re. Up to  $35^\circ$  angle of attack, the amplitude of the oscillations increased with angle of attack and beyond that angle, it reduced due to vortex breakdown. Oscillations completely vanished for angles of attack beyond  $55^\circ$ . Gupta<sup>20</sup> carried out experiments on  $65^\circ$  delta wing at NWTF, IIT Kanpur. He found that Re, in the range of  $1.6 \times 10^6$  to  $2.1 \times 10^6$ , had no significant effect over aerodynamic characteristics. He investigated two configurations, fuselage far from the wing apex and fuselage near the wing apex. The second configuration showed a tendency to increase the lift force coefficient and drag force coefficient. Yawing moment coefficient also had a tendency to increase but it was only up to  $20^\circ$  angle of attack. There was a decrease in the pitching moment and side force coefficients for all angles of attack before stall.

## ***1.2 Present Study***

The present study was motivated by the lack of details on the aerodynamic performance of the delta wing with  $75^0$  sweep angle. Extensive investigation was carried out to measure the aerodynamic forces and moments over the wing at static condition. In an effort to understand the flow characteristics over the surface of the wing and its influence on forces and moments smoke flow visualization was carried out. The effect of varying angles of attack and angles of sideslip was also studied.

The following chapters elaborate the experimental procedure and the instrumentation used in experiments. Results of the investigation are discussed in detail and correlated with the flow visualization results.

# EXPERIMENTAL ARRANGEMENT

Experiments were carried out at National Wind Tunnel Facility (NWTF), IIT Kanpur. Delta wing model was mounted inside the test section of the wind tunnel. Model was tested at constant wind speed (30 m/s). The model was mounted on Turntable. Rotation of the Turntable provided various angles of attack, and a 6-Component Strain Gage Balance was used to measure aerodynamic forces and moments on the model. Controlling the Turntable rotation and data acquisition was done using sophisticated instrumentation. Finally, smoke flow visualization was carried out using Laser Light Sheet Equipment to visualize the characteristics of the flow field over the surface of the model.

## ***2.1 Experimental Facility***

The National Wind Tunnel Facility (NWTF) at IIT Kanpur has been used to carry out the present investigation. It is a low speed closed circuit wind tunnel with associated equipment and modern instrumentation. It has interchangeable test sections having cross section  $3m \times 2.5m$ . The test section is split into two parts: an upstream and a downstream part. This facilitates four combinations of two upstream and two downstream parts. Length of the upstream part of the test section is 5.75m and that of the downstream part is 3m. Aerodynamic layout of the tunnel circuit is shown in figure 1, which elaborates its design features. Wide-angle diffuser with contraction ratio 9:1 is provided before the settling chamber. Maximum wind speed is 80m/s with Reynolds No.  $6 \times 10^6 / m$ . Free stream turbulence level is less than 0.1% and the maximum flow angularity is  $0.2^\circ$ . Wind is blown by a Fan & Drive system. The fan consists of a 12-bladed rotor followed by a 7-bladed stator and is driven by the 1000kW power, constant rated DC motor.

## **2.2 Model Description**

Geometric details of the delta wing model are shown in figure 3. The model was made up of a flat plate fabricated with aluminum. Its leading edge sweep was  $75^\circ$ . The length of the root chord was 1250mm with the span of 670mm at the trailing edge. The plate was of 10mm thickness and had sharp,  $30^\circ$  chamfered leading and trailing edges. Housing was provided near the trailing edge of the plate, which locked a 30mm diameter shaft. The shaft was manufactured with Alloy Steel EN8 and was hardened and grounded. The shaft protruded out of the trailing edge of the model by 200mm. This facilitated to hold the delta wing using elbows in a mounting setup. The model mounting setup using Turntable is shown in figure 4. The balance was mounted vertically on the Turntable using suitable balance rear end adapters. The turntable is of 2.4m diameter with rotation capability of  $0^\circ$  to  $360^\circ$ . Its accuracy is  $0.05^\circ$ . Model was mounted on the balance using balance front end adapters and cranked elbows. Model was fixed in  $90^\circ$ - roll angle configuration and its centerline was aligned to the direction of the wind flow. Turntable rotation provided the angle of attack variation. Sideslip ( $\beta$ ) was varied by using fabricated elbows having included angles  $80^\circ$ ,  $85^\circ$ ,  $90^\circ$ ,  $95^\circ$  and  $100^\circ$  which gave  $\beta$  as  $-10^\circ$ ,  $-5^\circ$ ,  $0^\circ$ ,  $5^\circ$  and  $10^\circ$  respectively.

## **2.3 Instrumentation**

The instruments used in the experiments are highly sophisticated and most advanced ones with which NWTF is equipped. All these instruments are actuated and controlled by Virtual Instruments. Software routines for VIs were developed in LabVIEW, which is described in chapter 3.

### ***Strain gauge Balance***

For measuring three orthogonal aerodynamic forces and three orthogonal aerodynamic moments on the model, a 6-Component strain gauge balance was used. The balance measured forces and moments in the balance axis coordinate system.

The balance comprises of flexible beam elements curved inside a cylindrical body, which is fabricated with Alloy Steel (EN24). It is of 60mm diameter and 425mm long with tapered ends. Strain gages, which sense the load acting on the balance and produce electrical output in milli-volt range, are fixed inside the balance body. The normal force and side force measuring gages are fixed symmetrical to the center at a distance of 0.065m. There are two axial force measuring elements placed on either side of the balance center point. All the bridges are configured as summing circuits. A summing circuit requires two gages placed on one side of the balance, which come under tension, and two on the other side, which come under compression. The balance was calibrated before it was used in experiments. More details about the balance specifications & load ranges, calibration procedure are given in the appendix.

### ***Data Acquisition Board***

A high speed Data Acquisition Board (DAQ Board) PCI-6034E with a frequency of 100Ksamples/s from National Instruments was used for data acquisition, which acts as an interface between the sensors and the computer. The data was acquired, digitized and transferred to the Virtual Instrument software routine by the DAQ board. The ADC has 16-bit resolution. With this board it is possible to scan 16 analog input channels at a maximum scan rate of 16 kHz. It has two 12-bit analog output channels, 8 digital I/O lines and two 24 bit counters. All connections to the data acquisition card are routed through the signal conditioning board SC-2043-SG.

### ***Signal Conditioning Unit***

The SC-2043-SG is an eight-channel signal conditioning board that interfaces the strain gage signal to the DAQ boards. Each terminal includes half-bridge completion with jumper disabled for full-bridge connections, sockets for quarter bridge completion resistors, and amplifier gain of 10. This signal conditioner provides buffered single pole 1.6 kHz filter, offset nulling circuit, and screw terminal connections to accommodate strain gage bridge measurements. Output voltage excitation leads and input signal leads

are attached at the voltage adjustment screws. An external excitation is provided and is common to all channels. The conditioned strain gage signals are routed to eight single ended analog inputs on the DAQ board.

### ***Free Stream Velocity Measurement***

The pressure difference ( $\Delta P$ ) across the contraction cone is related to the dynamic pressure ( $Q$ ) in the test section. The relationship is given by

$$\Delta P = KQ$$

where  $K$  ( $=0.883$ ) is the calibration constant obtained experimentally. During the experiment  $\Delta P$  is monitored using a digital manometer. The manometer can be configured as a local system or as a remote system. In the remote mode, the manometer is interfaced with the VI through RS 232 communication.

### ***Laser Light Sheet Equipment***

This equipment is used for smoke flow visualization. It consists of a system of Spectra Physics 6-watt Argon-Ion Laser with Multi mode Optic Fiber Link with Manipulator and Adapter. The sheet of Laser beam is emitted from oscillating mirror system and the sheet can be focused on either longitudinal plane or lateral plane. Fog generator is used for generating the flow of smoke and this smoke is emitted through a pipe, which is placed upstream of the apex of the model in the test section. The smoke flow can be visualized by focusing the laser sheet on the required plane over the flow. CCD cameras are placed at appropriate places to see and record the flow behavior in different directions.

## ***2.4 Force Measurement***

The model was mounted on the turntable with  $90^\circ$ -roll lock configuration. Tests were carried out to find the aerodynamic forces and moments acting on the model. The balance was mounted vertically on the turntable. Balance's positive side force was faced to wind. Balance measures 3 components of force (axial force, normal force and side force) and 3 components of moments (pitching moment, yawing moment and rolling moment). The



The balance measures the force with strain gages, which are placed inside its body. These are resistance type electric strain gages. For measuring normal and side forces two strain gages are placed on compression side and two strain gages are placed on tension side. All the four gages form the arms of a wheatstone full bridge circuit. The bridge gets excitation voltage from an external power supply. As force is applied the balance of the bridge circuit gets disturbed and the bridge emits voltage in the order of mV.

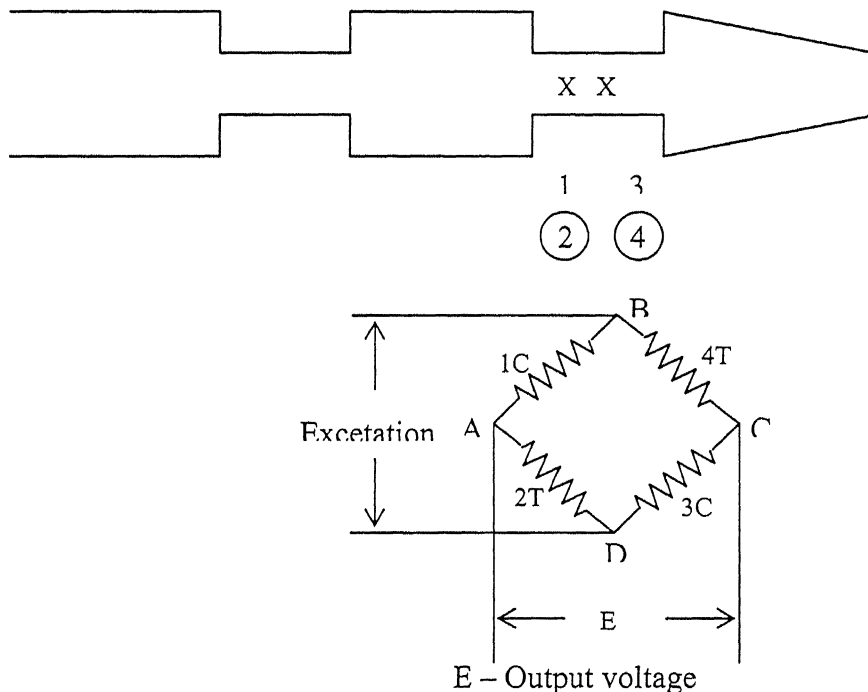
### *Strain gage*

Strain gages mounted in the balance are resistance type electric strain gages. Resistance of the wire increases with the strain applied to the wire. The resistance  $R$  of a uniform length  $L$ , cross section  $A$  and specific resistance  $S$  is given by

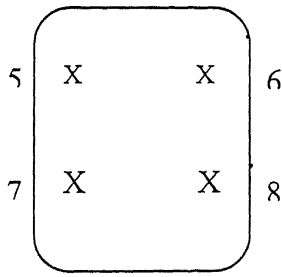
$$R = S \times L / A$$

Typical material used in strain gage construction is Constantan (45% Ni and 55% Cu) with strain sensitivity 2.1.

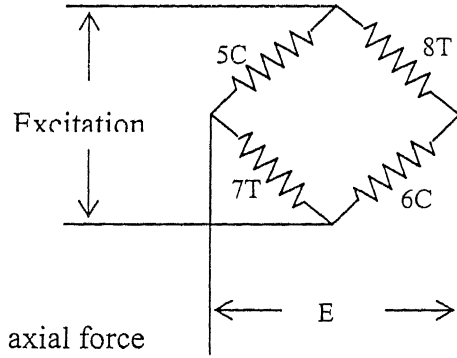
### *Wheatstone Bridge*



Bridge configuration for normal and side forces



Bridge configuration for axial force

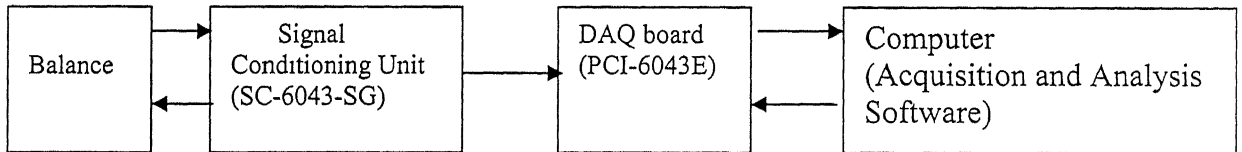


As shown in the above figures strain gages (1) and (3) are placed on compression side and (2) and (4) are placed on tension side. Excitation voltage is applied across B and D terminals and the out put voltage is collected across A and C terminals. Before the straining occurs the bridge is perfectly balanced and the following relation holds good:

$$\frac{R_1}{R_4} = \frac{R_2}{R_3}$$

In perfectly balanced state the output voltage is zero. After strains are applied resistance values change, thus the bridge is no longer balanced and the output voltage is not zero.

### *Force Measurement Chain*



The model was tested at 30m/s wind speed by varying the angle of attack from  $-10^\circ$  to  $61^\circ$  in steps of  $2^\circ$ , with a fixed sideslip angle. All bridges on the balance received the excitation voltage from a 5V constant power supply. The balance gave the data in the form of voltage signals. These signals were of the order of milli-volts and were amplified & filtered by SC-6043-SG signal conditioning board. The data was acquired and digitized by PCI-6034E DAQ board (more details of data acquisition are given in chapter 3).

The digitized data was analyzed by using a Virtual Instrument (VI) software routine. The VI was developed using LabVIEW software. Forces and moments in the balance axis coordinate system were measured by using the balance and further transformation was carried out to arrive at the aerodynamic behavior in the wind axis system.

## **Data Acquisition and Analysis**

During the experiment as wind flows over the model, the model is subjected to aerodynamic forces and moments. Strain gages, placed at appropriate locations on the balance, emit electric signals of the order of milli-volt range. These signals are taken to the signal conditioner where they are amplified and filtered. This data is acquired by the DAQ board, which resides inside the computer. The ADC digitizes the data and provides to the program as input. This digital information is analyzed by the program and presented in the graphs in an intelligible form to the user. The raw data is kept in a text file and is analyzed later to obtain the forces and moments at the balance axis. Further transformations of these forces and moments are carried out to arrive at the body axis and finally to the wind axis. Data acquisition is performed by the PCI-6034E DAQ board. For controlling the DAQ board and analyzing the data to present the results, programs are developed in LabVIEW software.

### **3.1 LabVIEW**

LabVIEW (Laboratory Virtual Instrument Engineering Workbench) is a program development environment, which uses graphical language, G, to create programs which are analogous to the programs developed in some other environments like C, BASIC. But unlike these programming environments, in which programs are written in text form, LabVIEW supports the programs in block diagram form. It uses terminology, icons and ideas to describe programming actions. In the program, a function executes only after the data is received by all of its input terminals. This is the data-flow principle, which governs the execution of the program in a straightforward manner. It comprises extensive libraries of functions for performing various programming tasks. It includes libraries for data acquisition, VXI, GPIB and Serial port Instrument control, data analysis, data presentation and data storage. It also includes conventional programming development tools, so one can set breakpoints, animate program execution to see how data passes through the program to make debugging and program development easier.

### 3.2 Data Acquisition

The front panel of the data acquisition program is shown in figure 7. Data acquisition is performed using PCI-6034E DAQ board. Specifications of this DAQ board are given in chapter 2. Voltage signals from all 6 strain gage bridges on the balance, after getting processed in signal conditioner, are received by ADC. Voltage signals represent varying forces acting on the model. Hence, the signal level and behavior over time are important phenomena. One thousand scans are acquired at the scan rate of 100 scans/sec. This amounts to 10 seconds of data. The acquisition duration can be varied by varying the number of scans or scan rate. At each angle of attack 10sec, 12sec and 15sec of data from 6 channels (Ax, N1, N2, S1, S2, Rm) and the excitation from the 7th channel are collected. This data is normalized with respect to excitation voltage. The time series of the normalized raw data (mV/V), along with the angle of attack, the wind speed and the dynamic head, is stored in a text file. At the beginning one set of no wind data is collected with 0° angle of attack. The data acquisition front panel is shown in figure 7.

### 3.3 Data Analysis

A typical data analysis routine is shown in figure 8. At each angle of attack, all the data points of each channel are averaged. The no wind data is subtracted from the wind data and the resulting vector, which contains the data points of all 6 channels at a particular angle of attack, is multiplied by the balance calibration coefficient matrix (matrix is shown in table 1, appendix-A) to obtain the forces, in Kg, acting on each channel. With these forces, aerodynamic forces and moments at the balance center (at location (1) as shown in figure 4) are derived using the following set of equations.

$$A_{x_{bal}} = A_x$$

$$N_{bal} = N1 + N2$$

$$S_{bal} = S1 + S2$$

$$M_{p_{bal}} = (N1 - N2) \times 0.065$$

$$M_{y_{bal}} = (S1 - S2) \times 0.065$$

$$M_{r_{bal}} = R_m$$

The forces/moments from location (1) are transformed to location (2), which is the intersecting point of the balance axis and the axis of the model.

Transformation equations from location (1) to location (2) are:

$$NF1 = -N_{bal}$$

$$SF1 = A_{x_{bal}}$$

$$A_{x1} = -S_{bal}$$

$$M_{p1} = -M_{r_{bal}}$$

$$M_{y1} = M_{y_{bal}} - S_{bal} \times 0.4$$

$$M_{r1} = -M_{p_{bal}} + N_{bal} \times 0.4$$

From location (2), the aerodynamic forces/moments are taken to body axis system, whose reference point is the geometric center of the model (location (3)) and finally they are transformed to wind axis system.

From location (2) to body axis transformation:

$$NF_b = NF1$$

$$SF_b = SF1 \times \cos \beta - A_{x1} \times \sin \beta$$

$$A_{x_b} = A_{x1} \times \cos \beta + SF1 \times \sin \beta$$

$$M_{p_b} = M_{p1} \times \cos \beta - 0.72 \times NF1 - R_{m1} \times \sin \beta$$

$$M_{y_b} = M_{y1} - 0.72 (SF1 \times \cos \beta + A_{x1} \times \sin \beta)$$

$$M_{r_b} = M_{r1} \times \cos \beta + M_{p1} \times \sin \beta$$

Body axis to wind axis transformation:

$$D_w = A_{x_b} \times \cos \alpha \times \cos \beta - NF_b \times \sin \alpha \times \cos \beta + SF_b \times \sin \beta$$

$$L_w = NF_b \times \cos \alpha - A_{x_b} \times \sin \alpha$$

$$Y_w = SF_b \times \cos \beta + A_{x_b} \times \cos \alpha \times \sin \beta - NF_b \times \sin \alpha \times \sin \beta$$

$$M_{p_w} = M_{p_b} \times \cos \beta + M_{r_b} \times \cos \alpha \times \sin \beta + M_{y_b} \times \sin \alpha \times \sin \beta$$

$$M_{y_w} = M_{y_b} \times \cos \alpha - M_{r_b} \times \sin \alpha$$

$$M_{r_w} = M_{r_b} \times \cos \alpha \times \cos \beta + M_{y_b} \times \sin \alpha \times \cos \beta - M_{p_b} \times \sin \beta$$

Aerodynamic coefficients of forces & moments are derived as follows and are plotted in graphs to obtain the aerodynamic characteristics of the  $75^0$  delta wing.

Non-dimensional coefficients:

$$C_L = L_w / (Q \times S)$$

$$C_D = D_w / (Q \times S)$$

$$C_Y = Y_w / (Q \times S)$$

$$C_{mp} = M_{p_w} / (Q \times S \times C)$$

$$C_{my} = M_{y_w} / (Q \times S \times b)$$

$$C_{mr} = M_{r_w} / (Q \times S \times b)$$

Where

Surface area of the wing (S) =  $0.417 \text{ m}^2$

Root chord (C) = 1.25m

Wing span along the reference point (b) = 0.447 m

## RESULTS AND DISCUSSION

The model was tested in static condition at a constant wind speed of 30 m/s which corresponds to  $Re$  of  $1.6 \times 10^6$ . The model was locked with  $90^\circ$ -roll angle and its root chord was properly aligned with the axis of wind flow. Angle of attack ( $\alpha$ ) was varied from  $-10^\circ$  to  $61^\circ$  in steps of  $2^\circ$  for each sideslip angle ( $\beta$ ). Tests were carried out with  $\beta$  fixed at  $-10.75^\circ$ ,  $-5.75^\circ$ ,  $0^\circ$ ,  $4.6^\circ$ , and  $10.12^\circ$ . The balance, which was used for measuring the forces and moments, gave the results in balance axis coordinate system. These results were resolved to wind axis system and were shown in graphs. The reference point for moments was taken at 2/3rd chord length from the apex of the model. Smoke flow visualization and laser sheet technique were used to study the structure of leading edge vortices as they broke down. A combination of lateral and longitudinal laser cross-sectional views provided information on the three dimensional nature of the vortex structure before, during, and after breakdown.

The following paragraphs explain the effect of  $\alpha$  and  $\beta$  on the aerodynamic characteristics of the wing and correlate the results with the results of smoke flow visualization.

### **4.1 Effect of Angle of Attack ( $\alpha$ )**

The model was tested at different angles of attack to investigate the effect of  $\alpha$  on the aerodynamic characteristics of the delta wing. The variation of all aerodynamic coefficients with the angle of attack for  $0^\circ$  sideslip angle is shown in figure 10. The trend of the lift coefficient ( $C_L$ ) is as expected. Maximum lift coefficient ( $C_{L,max}$ ) attained is 1.43 at  $34^\circ$  angle of attack. Lift coefficient ( $C_L$ ) starts falling beyond  $\alpha = 34^\circ$  as stall occurs. The cause of this phenomenon was well explained by Polhamus<sup>2</sup> leading edge suction analogy. Theoretically, total lift over the slender wings with high sweep angles is considered to be the sum of the potential lift and vortex lift. Well organized leading edge vortices have high axial velocity at its center, where the pressure is very low. These



regions are the sources of enormous suction, created over the upper surface of the wing. This suction, as long as it exists, causes vortex lift. As the angle of attack increases vortices start breaking down, leading to the condition for stall. After breakdown suction effect over the wing upper surface decreases, consequently vortex lift gets reduced.

Drag coefficient increases sharply beyond  $\alpha = 5^\circ$  and reaches the maximum value of 1.02. It appears to fall at  $\alpha = 35^\circ$  but beyond that angle it rises sharply. In the region after the vortex burst location, the flow becomes violently turbulent which causes decrease in  $C_D$ . Drag force always accompanies lift. In the design of aircraft optimum L/D ratio, which is also known as aerodynamic efficiency, is taken. Figure 11, which shows the drag polar, provides substantial information in this regard. Figure 14 gives the pitching moment coefficient variation with  $\alpha$  at  $0^\circ$  sideslip. For angles of attack beyond  $15^\circ$  vortices at the rear end of the wing lift off the surface where vortex lift reduces. This phenomenon creates force imbalance along the root chord, which causes the positive pitching moment. Maximum pitching moment is at  $34^\circ$  angle of attack. After stall occurs, imbalance in the lift gets reduced hence the curve falls.

Variation of  $C_Y$  and  $C_{ym}$  are shown in figures 13 and 15 respectively. At  $0^\circ$  sideslip angle the yaw force coefficient ranges between -0.005 & 0.065 with increased angle of attack. After stall occurs,  $C_Y$  falls sharply. Interestingly for  $\alpha$  beyond  $10^\circ$ , high negative yaw coefficients were observed at high positive yaw angles and vice versa. This was well explained by Stahl<sup>13</sup>. He found that the effective sweep back angle increases with  $\alpha$  at which vortex breakdown occurs. For positive high angles, effective sweep back angle on the right side of the wing is higher. So, at moderate and high angles of attack the left vortex remains attached to the surface whereas the vortex on the right side lifts up from the surface causing sidewash. Due to this sidewash negative side force appears.  $C_{rm}$  is found to be negative for the entire range of  $\alpha$  as shown in figure 16. At low angles of attack the asymmetry in the two leading edge vortices cause a slight rolling moment. It was observed in the smoke flow visualization that as  $\alpha$  increases the left vortex starts breaking down while the right vortex retains its strength. This is the reason for negative

$C_{mr}$ . After  $\alpha = 34^\circ$ , as shown in figure 6 at  $0^\circ$  sideslip, the right vortex also breaks down causing a slight rise in the rolling moment coefficient.

## 4.2 Effect of Side Slip Angle ( $\beta$ )

The model was tested with sideslip angles ( $\beta$ )  $-10.75^\circ$ ,  $-5.75^\circ$ ,  $0^\circ$ ,  $4.6^\circ$ , and  $10.12^\circ$  in an effort to understand the effect of  $\beta$  on the aerodynamic forces and moments. Figures 21 to 26 show the variation of aerodynamic characteristics with  $\beta$ , keeping  $\alpha$  as parameter. Figure 21 shows the  $C_L$  variation with  $\beta$ . For  $\alpha$  up to  $20^\circ$   $C_L$  shows very low changes with  $\beta$ . But at higher angles of attack its variation is quite high. Lift coefficient ( $C_L$ ) drops by 0.265 at  $\beta = -10.75^\circ$ . The drop in the lift is found to be more with negative sideslip angles than with positive  $\beta$ . This change in lift can be expected from the fact that at some angle of sideslip one of the vortices moves out from the surface in lateral direction and hence the vortex lift reduces. Drag coefficient ( $C_D$ ) also shows similar trend as shown in figure 22. It decreases by 0.22 at  $-10.75^\circ$  sideslip angle. For lower angles of attack ( $\alpha$  less than  $20^\circ$ ) the variation of  $C_D$  with sideslip is very low. With the increase of  $\beta$ ,  $C_D$  increases and  $C_L$  decreases. The same trend continues for all angles of attack after the stall. Variations of  $C_Y$  &  $\Delta C_{my}$  with  $\beta$  are shown in figures 23 and 25 respectively. Both the yaw force and the yaw moment show considerable changes with  $\beta$ . As explained earlier  $C_Y$  and  $C_{my}$  are negative for positive sideslip angles and positive for negative angles. Figure 24 shows that  $C_{mp}$  is quite insensitive to the sideslip angle. Rolling moment coefficient ( $C_{mr}$ ) is positive for low angles of attack but always negative at all  $\alpha$  and  $\beta$  at higher angles of attack. Variation of  $C_{mr}$  is shown in figures 26.

## 4.3 Flow Visualization Results

A tube of smoke introduced upstream of the flow over the model impinges on the apex of the delta wing and is entrained into vortices. Vortex cross-sections are illuminated by passing the laser beam through a lens that splits it into a thin sheet or plane of light. With this arrangement both lateral and longitudinal planes are viewed.

The model is fixed with  $90^\circ$ -roll configuration and aligned to the wind flow. Sideslip angle is kept constant at  $0^\circ$ . The experiment is carried out starting with  $30^\circ$  angle of attack. At this angle the vortex on the left side moves away from the surface of the wing and breaks down somewhere downstream while the right vortex remains attached to the wing surface. This obviously creates asymmetry in the two vortices, which causes negative rolling moment. This is shown in figure 16. But as the two vortices are coherent all along the edges, lift and drag are not affected. As the angle of attack increases, the breakdown location of the left vortex moves upstream causing further imbalance which enhances the negative rolling moment. Exactly at  $35^\circ$  angle of attack the right vortex also breaks down and breakdown location suddenly moves upstream and appears at approximately  $2/3^{\text{rd}}$  of the root chord length. This phenomenon suddenly reduces the suction effect over the wing surface, which results in sudden drop in vortex lift<sup>2</sup>. This causes sudden downward jump in lift curve as shown in figure 10. Angle of attack is increased to  $40^\circ$ . At this angle breakdown location moved to almost  $1/3^{\text{rd}}$  chord length (from the apex). The flow over the wing surface is turbulent. This causes further reduction in the lift and rise in the drag. As the right vortex also breaks down like the left one, the imbalance gets moderated which moves the rolling moment coefficient curve (shown in figure 16) slightly up.

# Conclusions and Scope for Future Work

## 5.1 Conclusions

Aerodynamic characteristics of  $75^\circ$  delta wing were investigated at a constant wind speed of 30m/s, keeping the model in static condition. By conducting the experiments to find aerodynamic forces & moments and correlating the results with the results of flow visualization, various facts influencing the characteristics of delta wing have been obtained. The main observations are summarized below:

1. Location of vortex breakdown moves upstream suddenly at  $35^\circ$  angle of attack with  $0^\circ$  sideslip angle configuration that leads to sudden decrease in the lift.
2. Lift coefficient and drag coefficient decrease with sideslip angle at higher angles of attack (for all angles of attack beyond  $20^\circ$ ).
3. Pitching moment coefficient is fairly invariant with sideslip angle.
4. Yaw force and yawing moment are positive for all angles of attack with positive sideslip angle, while they are negative for angles of attack beyond  $10^\circ$  with all negative sideslip angles.
5. Rolling moment is always negative at all positive angles of attack with both positive and negative sideslip angles.
6. Rolling moment coefficient changes significantly with sideslip angle. It is negative for all angles of attack and sideslip angles.

## ***5.2 Scope for Future Work***

Considerably high variation of lift and drag coefficients with sideslip angle ( $\beta$ ) at  $\alpha$  beyond  $10^\circ$ , variation of yaw force, yawing moment & rolling moment coefficients with sideslip angle produce undesirable changes in the stability of the aircraft. This behavior limits the operating range of the angle of attack for delta wing. Hence, further research is proposed in modifying this adverse behavior. Wing rock can be observed by testing the model with free to roll configuration. Unsteady pressure distribution over the delta wing can be studied.

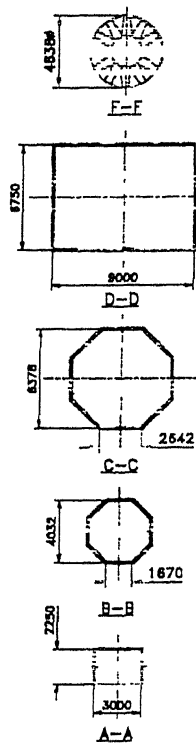
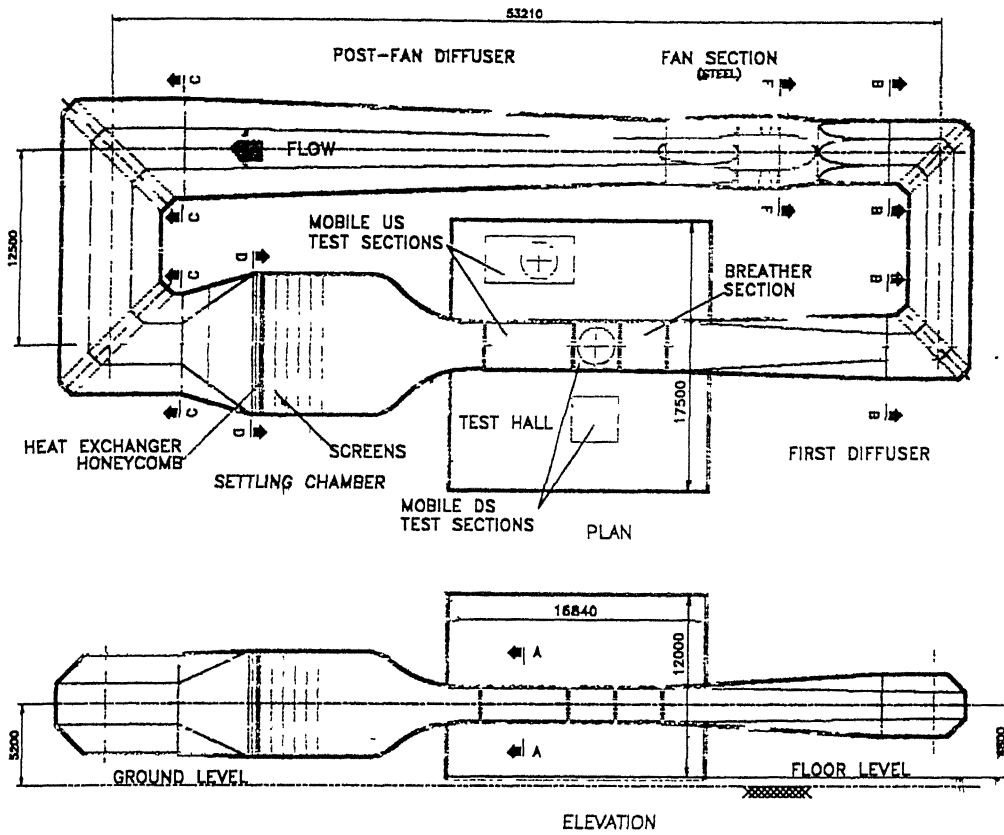
## References

1. Elle, B. J., and Jones, J. P., "A Note on the Vorticity Distribution on the Surface of Slender Delta Wing with Leading Edge Separation", Journal of the Royal Aeronautical Society, Vol. 65, March 1961, pp.195-198.
2. Polhamus, E. C., "A Concept of the Vortex Lift of Sharp-Edge Delta Wings Based on a Leading-Edge Suction Analogy", NASA TN D-3767 Oct. 1966
3. Lamar, J. E., "Subsonic Vortex-Flow Design Study for Slender Wings," Journal of Aircraft, Vol. 15, No.9, 1978, pp. 611-617.
4. Seginer, A., and Salomon, M., "Performance Augmentation of a 60-Degree Delta Aircraft Configuration by Span wise Blowing", Journal of Aircraft, Vol.23, Nov 1986, pp.801-807
5. Ericsson, L. E., and Redding, J. P., "Unsteady Aerodynamics of Slender Delta Wings at Large Angles of Attack", Journal Aircraft, Vol.12, No. 9, Sept. 1975, pp. 721-729.
6. Nguyen, L.E., and Yip, L.P., "Self Induced Wing Rock of Slender Delta Wings", AIAA Paper 81-1883, Aug 1981.
7. Levin, D., and Katz. I., "Dynamic Load Measurements with Delta Wings Undergoing Self-Induced Roll Oscillations", Journal of Aircraft, Vol. 21, No. 1, 1984, pp. 322-328.
8. Ericsson, L.E., "The Fluid Mechanics of Slender Wing Rock", Journal of Aircraft, Vol. 21, No. 5, May 1984, pp. 322-328.
9. Ng, T. Terry, Gerald, N., Malcolm and Liane, C., Lewis, "Experimental Study of Vortex Flows Over Delta Wings in Wing Rock Motion", Journal of Aircraft, Vol. 29, No. 4, Aug 1992, pp. 598-603.
10. Wentz, W.H., and Kohlman, D.L., "Vortex Breakdown on Slender Sharp Edged Wings", Journal of Aircraft, Vol. 8, No. 3, 1971, pp. 156-161.

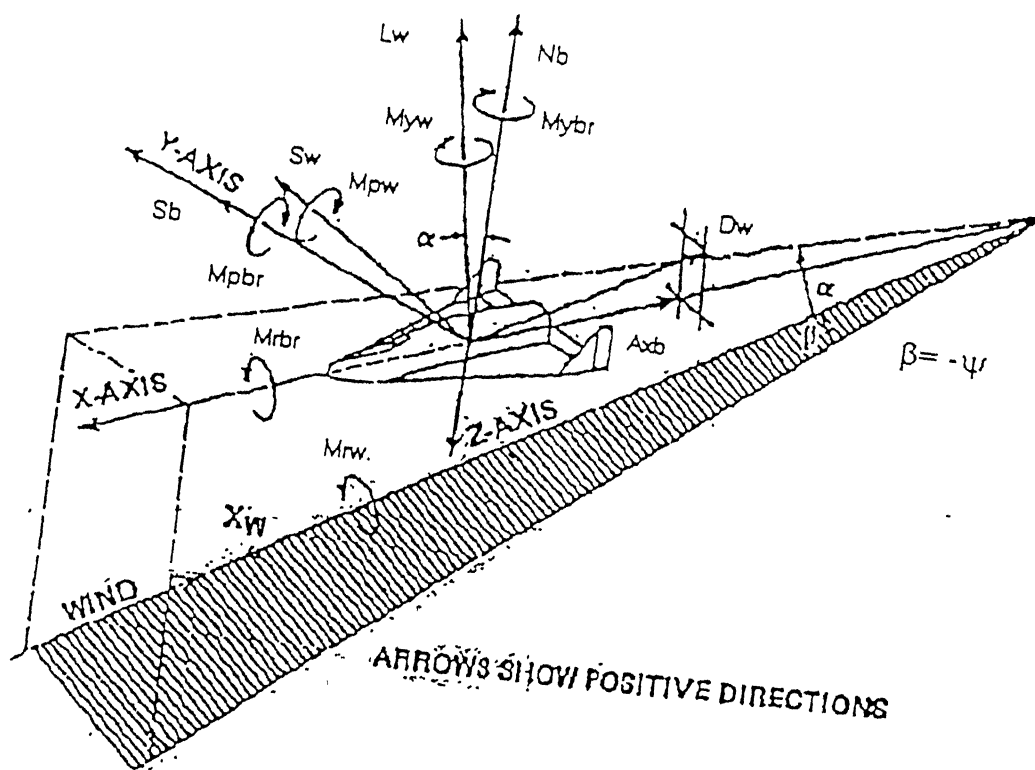
11. Payne, F. M., Ng, T. T., and Nelson, R.C., "Visualization and Wake Surveys of Vortical Flow over a Delta Wing", AIAA Journal, Vol. 26, No. 2, 1988, pp. 137-143.
12. Roos, F., and Kegelmann, J.T., "An Experimental Investigation of Sweep-Angle Influence on Delta Wings Flows", AIAA paper 90-0383, Jan 1990.
13. Stahl, W.H., "Experimental Investigations of the Vortex Flow on Delta Wings at High Incidence", AIAA Journal, Vol. 30, Apr 1992, pp. 1584-1586.
14. Lee, M., Shih, C., and Ho, C. M., "Response of Delta Wing in Steady and Unsteady Flows", ASME 1987, pp. 19-24.
15. Lance, W. T., and Brian, M., "Low-Reynolds-Number Effects on Delta-Wing Aerodynamics", Vol. 35, Journal of Aircraft, July-Aug 1998, pp. 653-656.
16. Weinberg, Zvi, "Effect of Tunnel Walls on Vortex Breakdown Location over Delta Wing", AIAA Journal, Vol. 30, No.6, June 1992, pp. 1584-1586.
17. Poddar, K. and Singh, M., "An Experimental Study of Vortex Break-down on a Delta Wing", Proceedings 23rd National Conference of Fluid Mechanics and Fluid Power, 27-29 Dec, 1996, PP. 86-94.
18. Sinha, K. Nandan, "Control of Vortex Breakdown of Flow Over a Delta Wing", an M.Tech. thesis, IIT Kanpur, July 1998.
19. Chattopadhyay, S., "Control of Wing Rock motion on an  $80^{\circ}$  Delta Wing", an M.Tech. thesis, IIT Kanpur, Mar 2000.
20. Gupta Amit, "Aerodynamic Forces and Moments Over a  $65^{\circ}$  Delta Wing", an M.Tech. thesis, IIT Kanpur, Feb 2001.

# Figures





AERODYNAMIC LAYOUT  
OF TUNNEL CIRCUIT



Body Axis to Wind Axis Transformations

Figure 2 Axis system

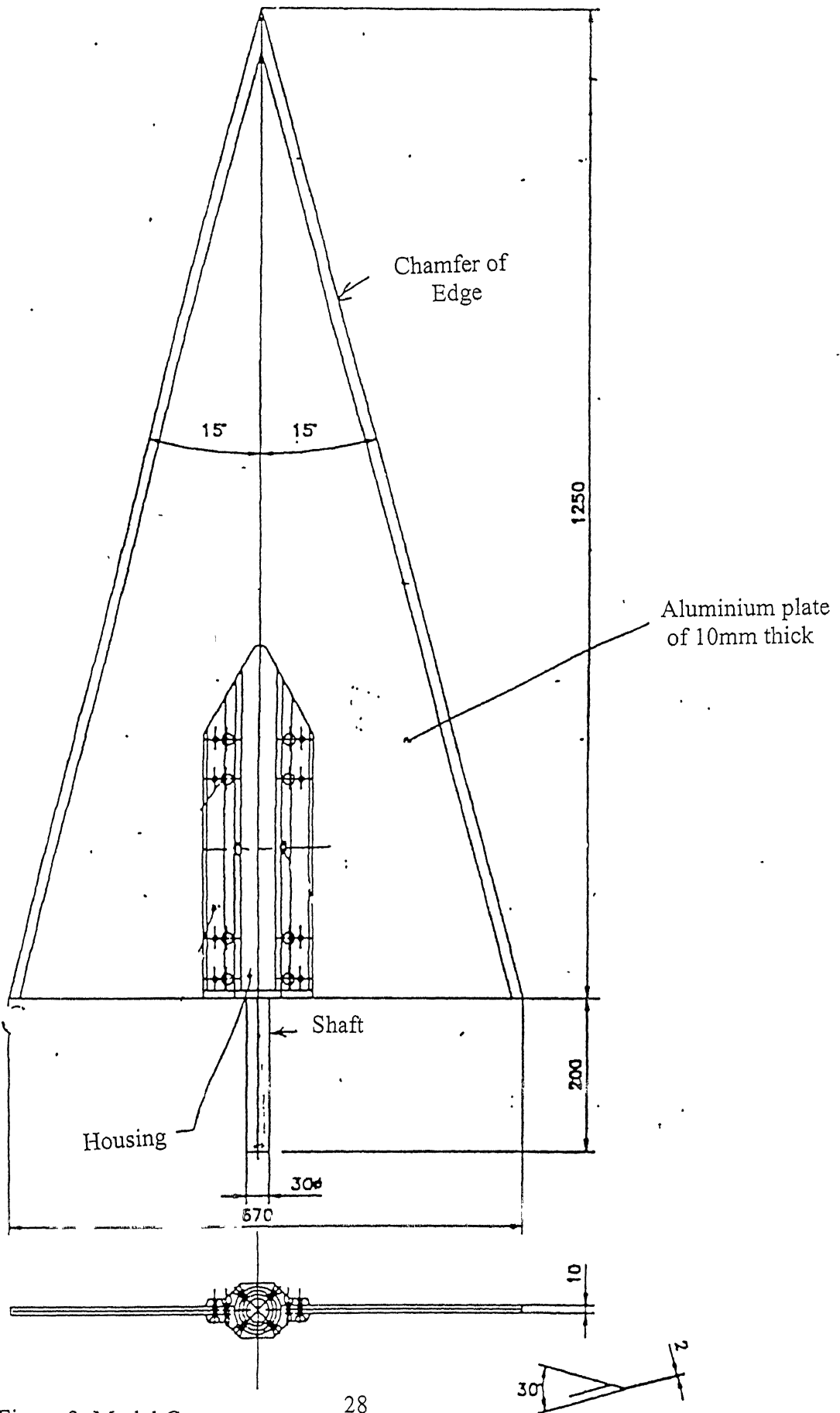


Figure 3: Model Geometry

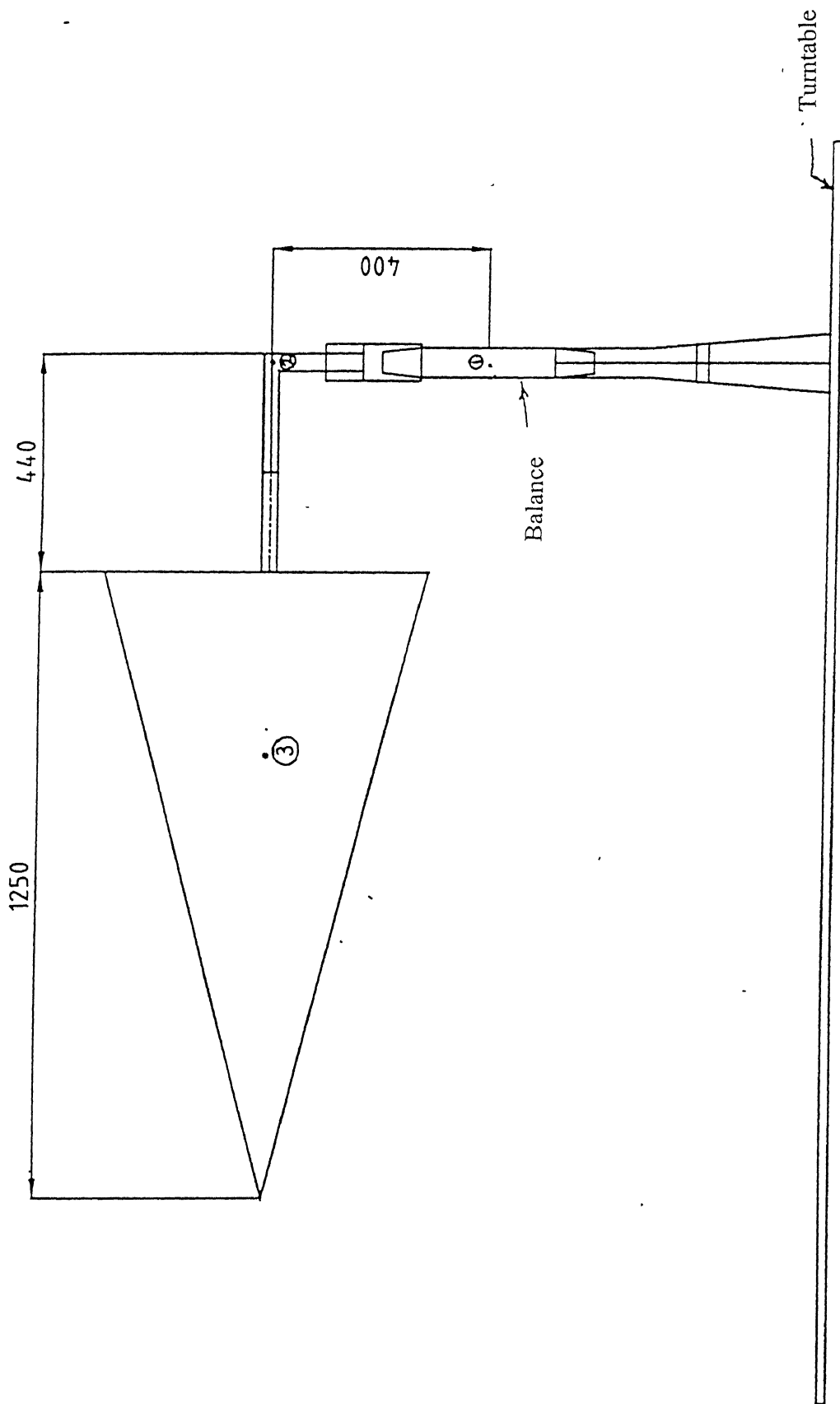


Figure 4

DELTA WING MOUNTED ON TURNTABLE (IN 90° ROLL CONFIGURATION)

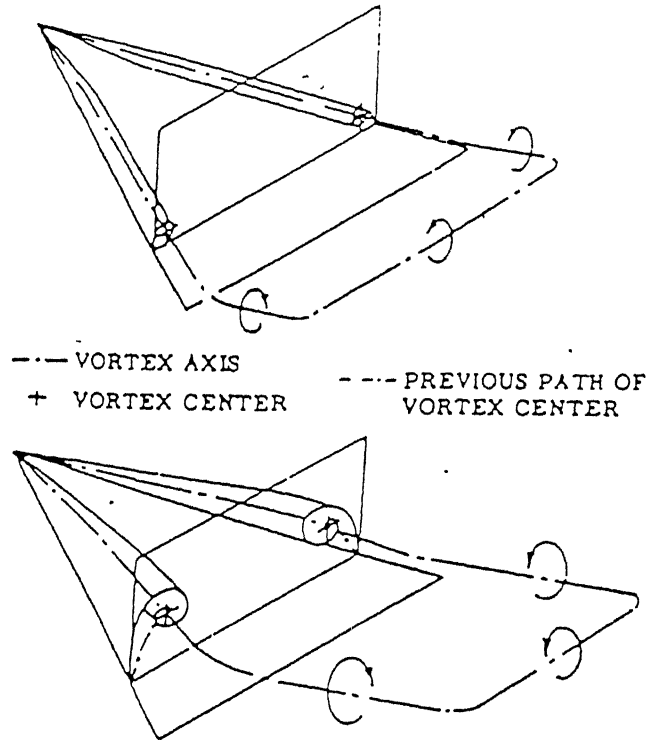


Figure 5:  
 SCHEMATIC REPRESENTATION OF FLOW  
 DURING PLUNGE FROM ZERO TO POSITIVE  
 INCIDENCE

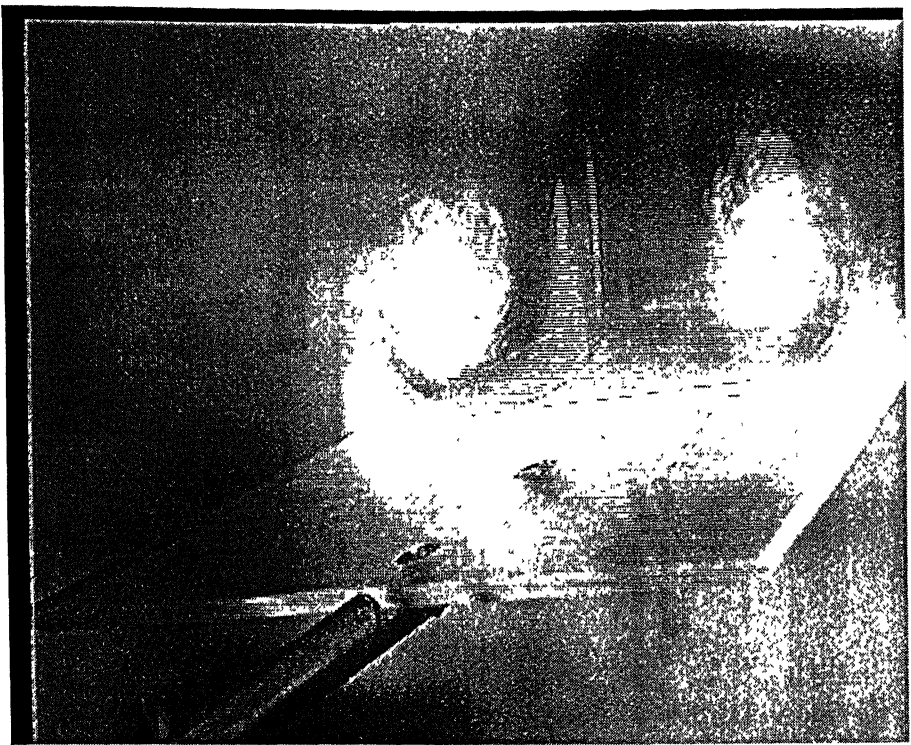


Figure showing two leading edge vortices

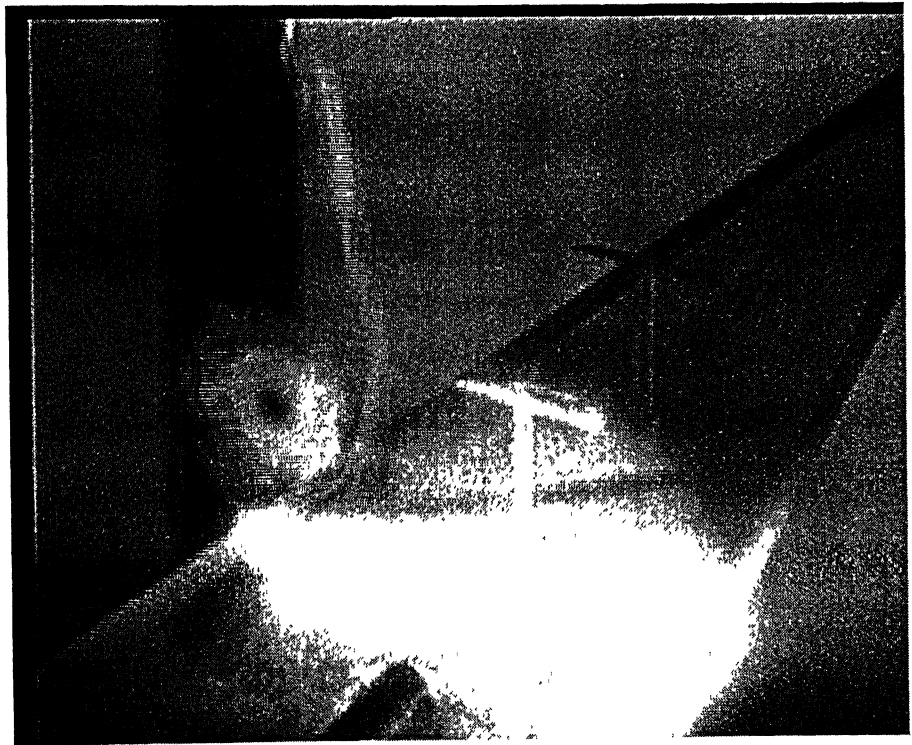


Figure showing breakdown of one of the vortices  
Figure 6

## DAQ Parameters

Device:

Scan rate:

Nscans:

Input limits:

high limit (0.0):

low limit (0.0):

File header

Delta Wing Mounted  
vertically with a  
vertical balance

Next set



STOP

## Motion Parameters

Motion Device:

Target angle:

Current angle:

Qmf:

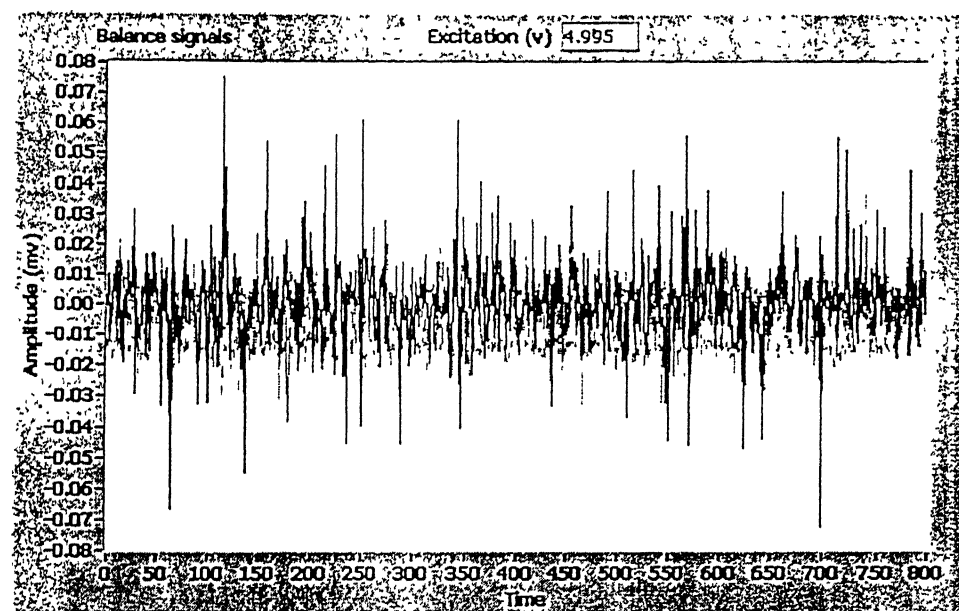
Unf:

Bridge output (mv/v)

Ax	N1	N2	S1	S2	Rm
0.001	-0.004	0.001	-0.014	-0.001	0.003

Bridge output (Kg)

Ax	N1	N2	S1	S2	Rm
0.000	0.000	0.000	0.000	0.000	0.000



Ax  
N1  
N2  
S1  
S2  
Rm

Figure 7 : Front panel of the data acquisition program

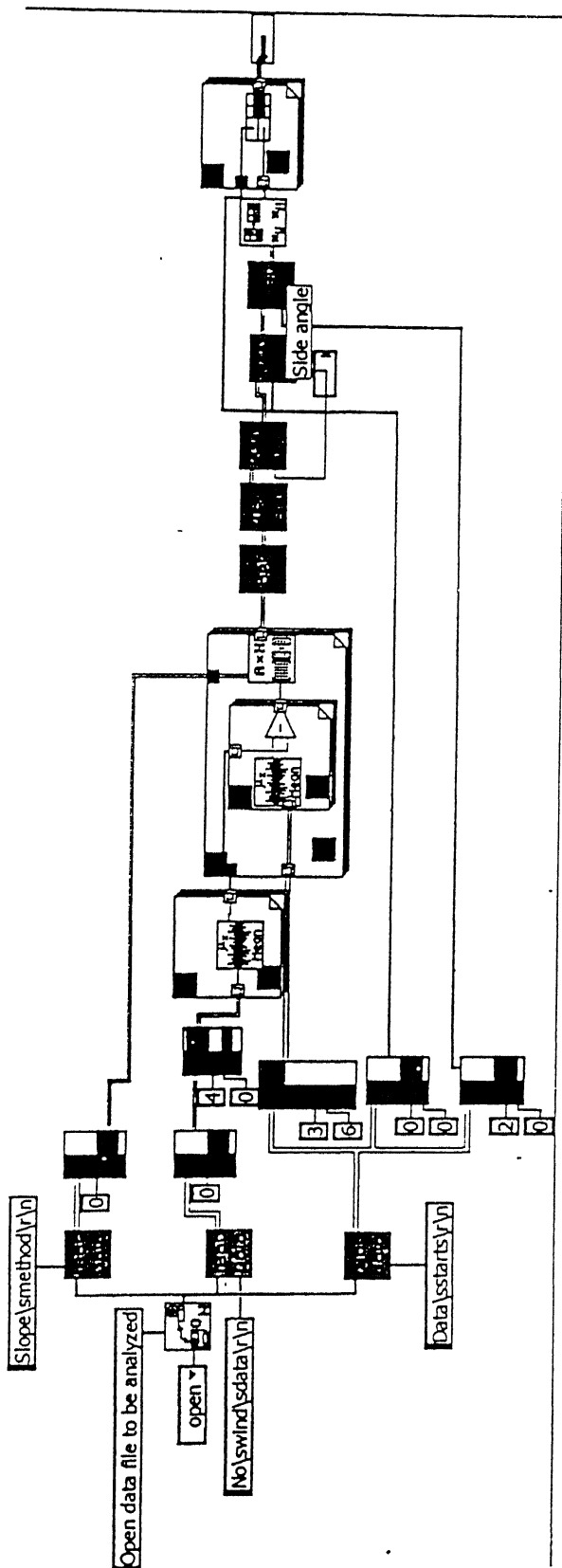


Figure 8: Block Diagram of Data Analysis



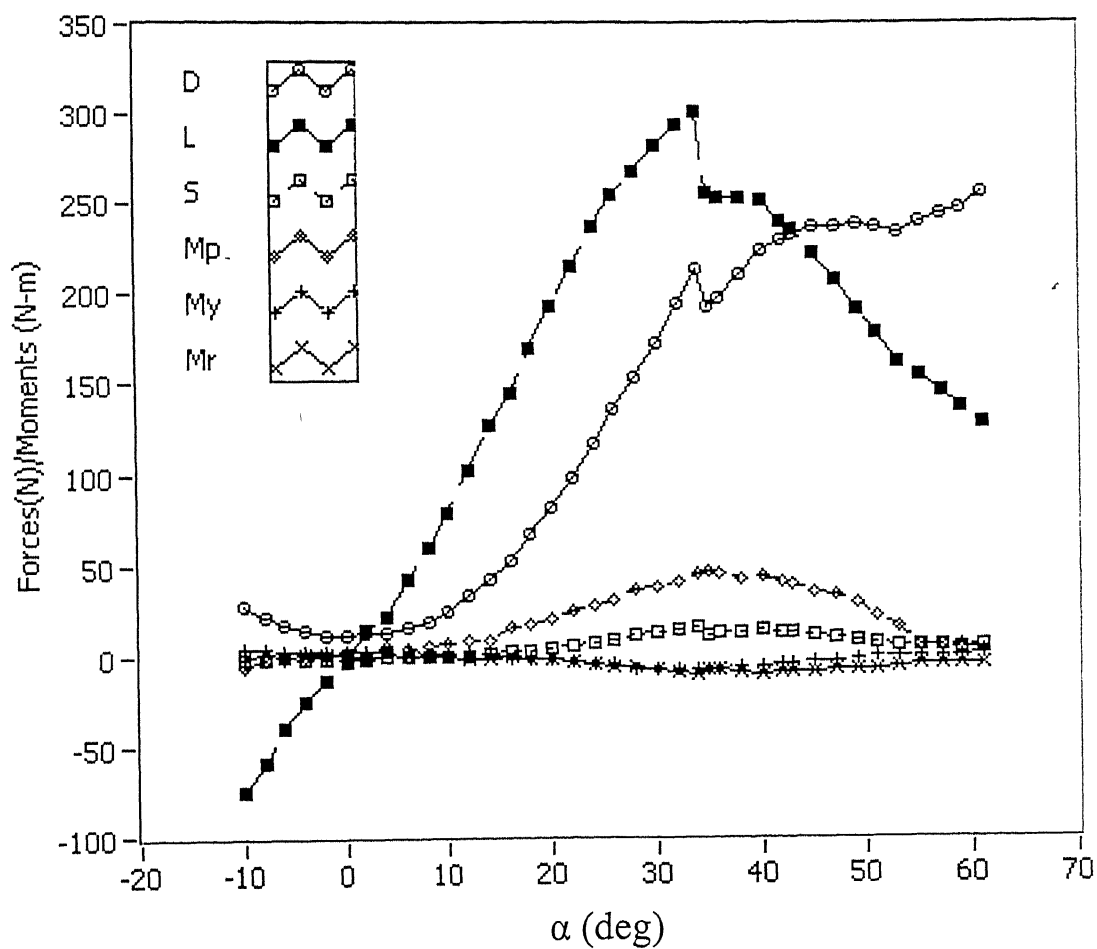


Figure 9: Variation of all aerodynamic forces and moments with angle of attack (with  $\beta$  as  $0^\circ$ )

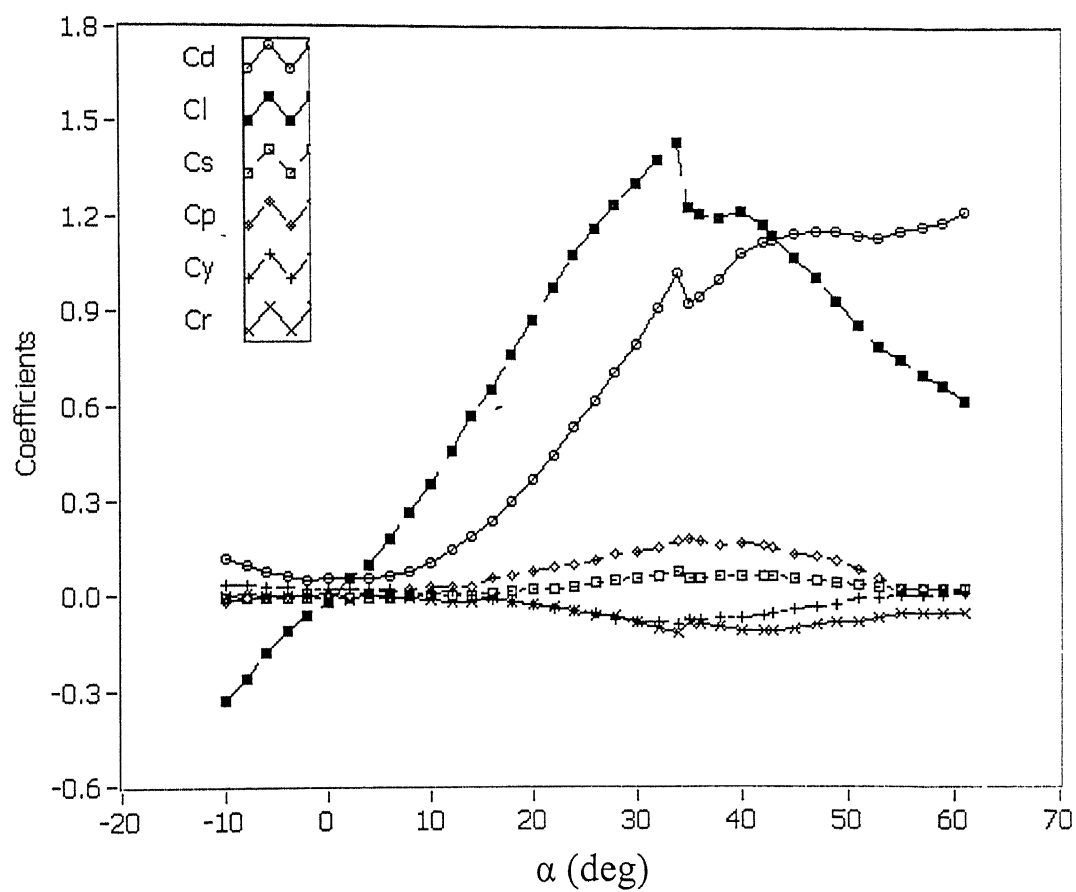


Figure 10: Variation of all aerodynamic coefficients with angle of attack (with  $\beta$  as  $0^\circ$ )

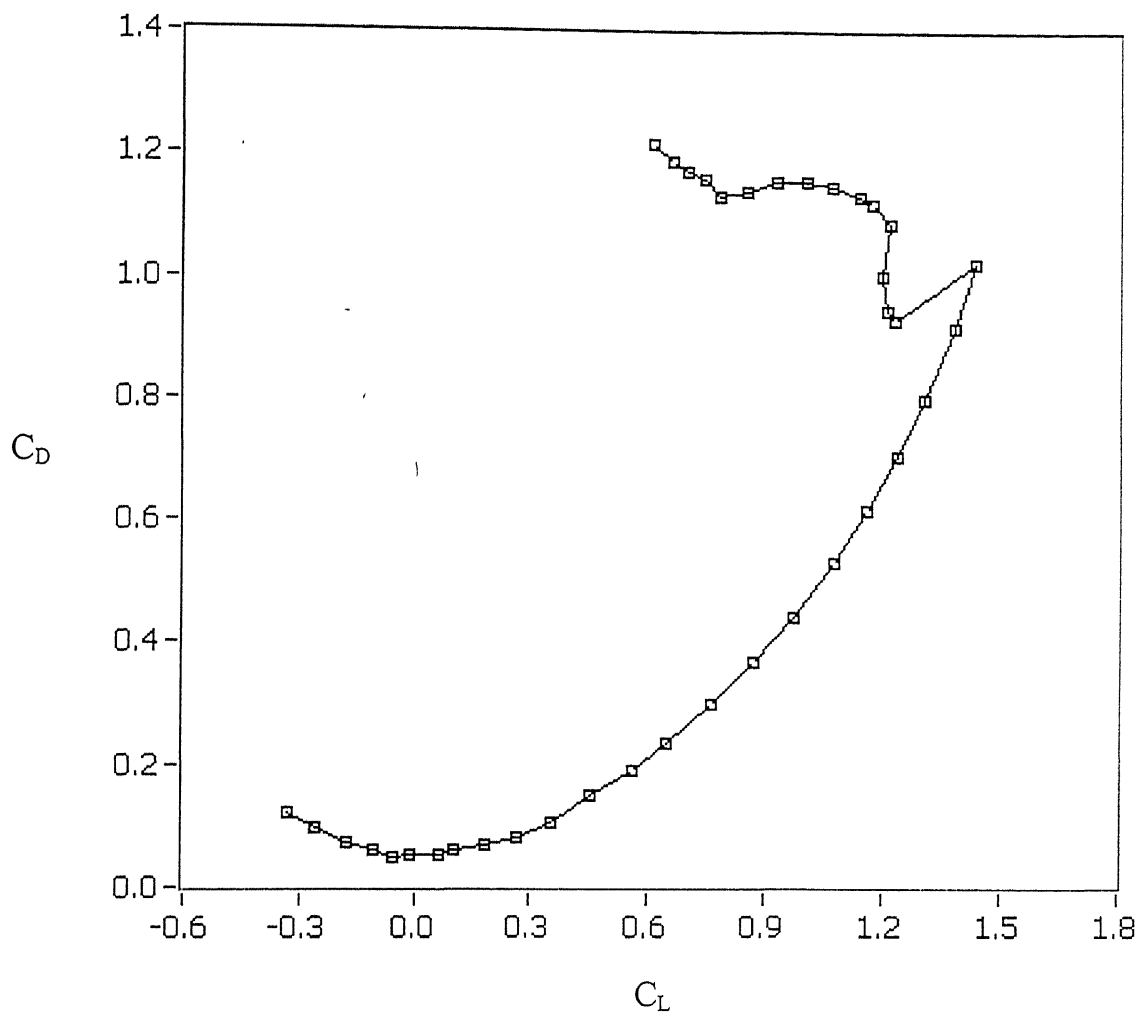


Figure 11: Variation of drag coefficient ( $C_D$ ) with lift coefficient ( $C_L$ ) at zero sideslip angle

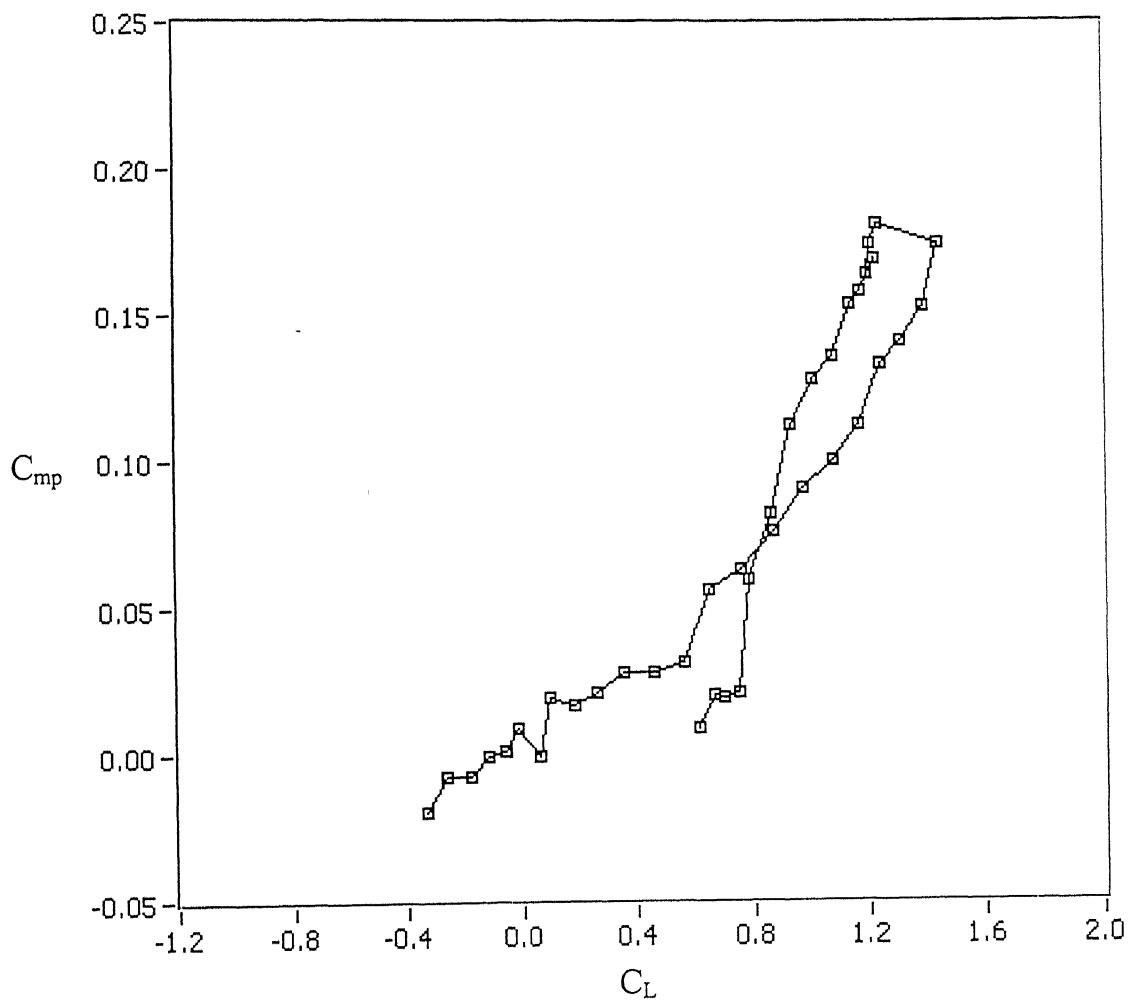


Figure 12: Variation of pitching moment coefficient ( $C_{mp}$ ) with lift coefficient ( $C_L$ ) at zero sideslip angle

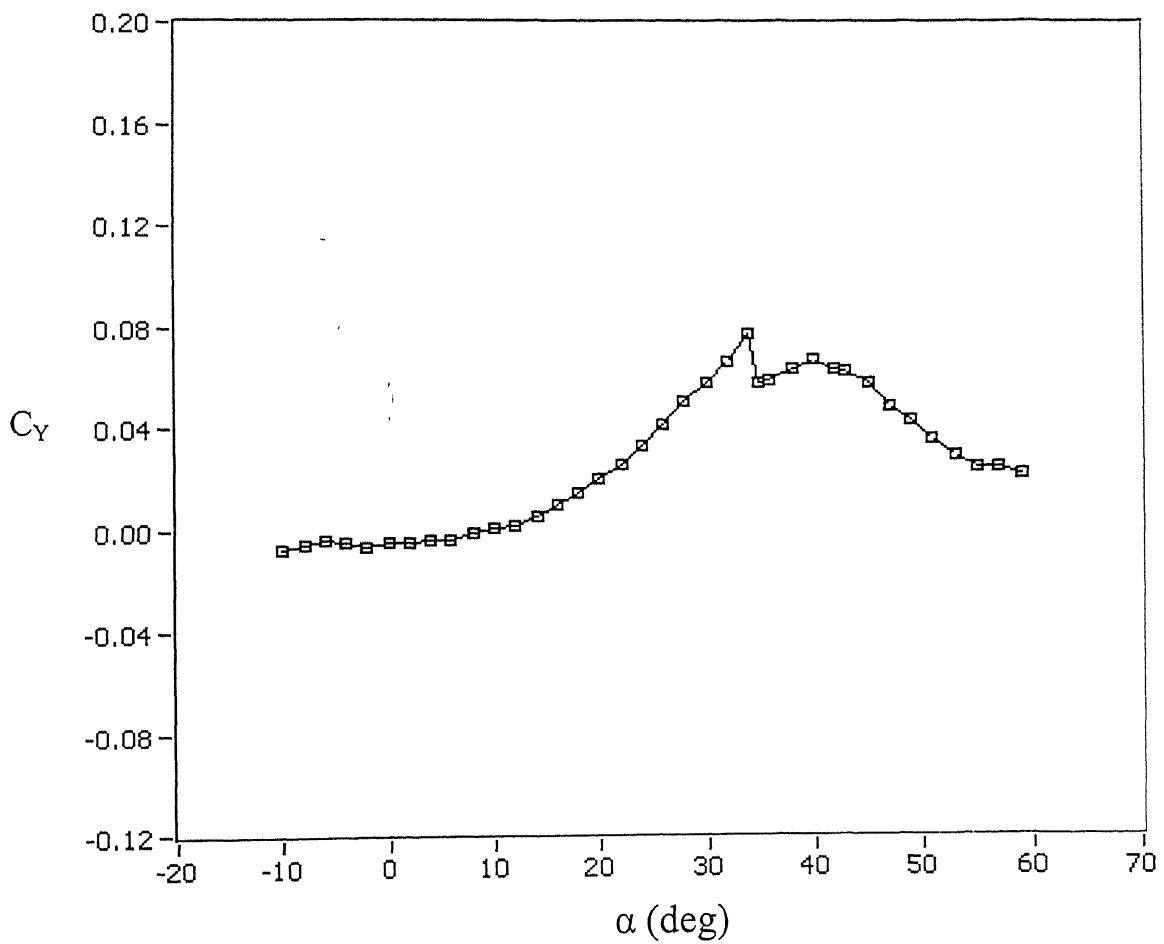


Figure 13: Variation of the side force coefficient ( $C_Y$ ) with angle of attack at  $\beta = 0^\circ$

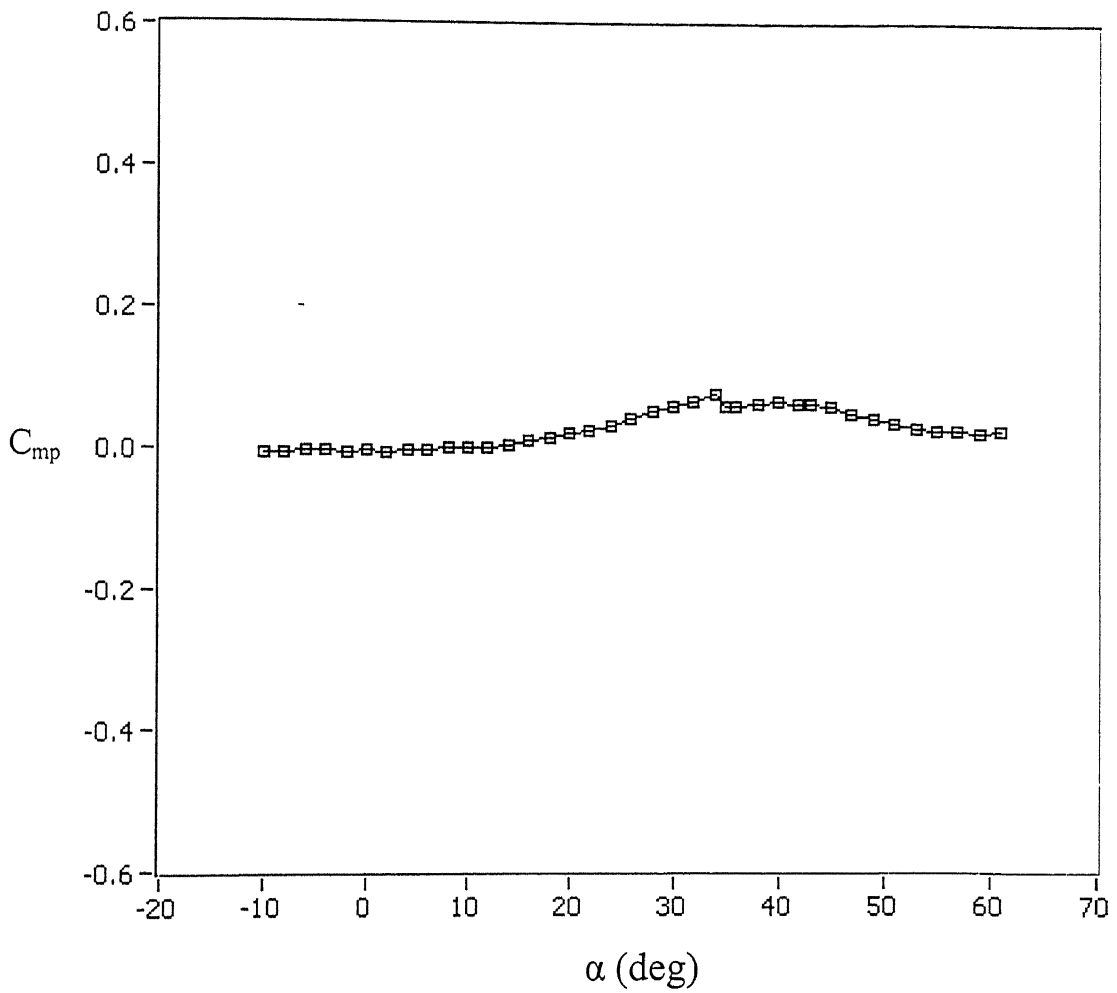


Figure 14: Variation of the pitching moment coefficient ( $C_{mp}$ ) with angle of attack at  $\beta = 0^\circ$

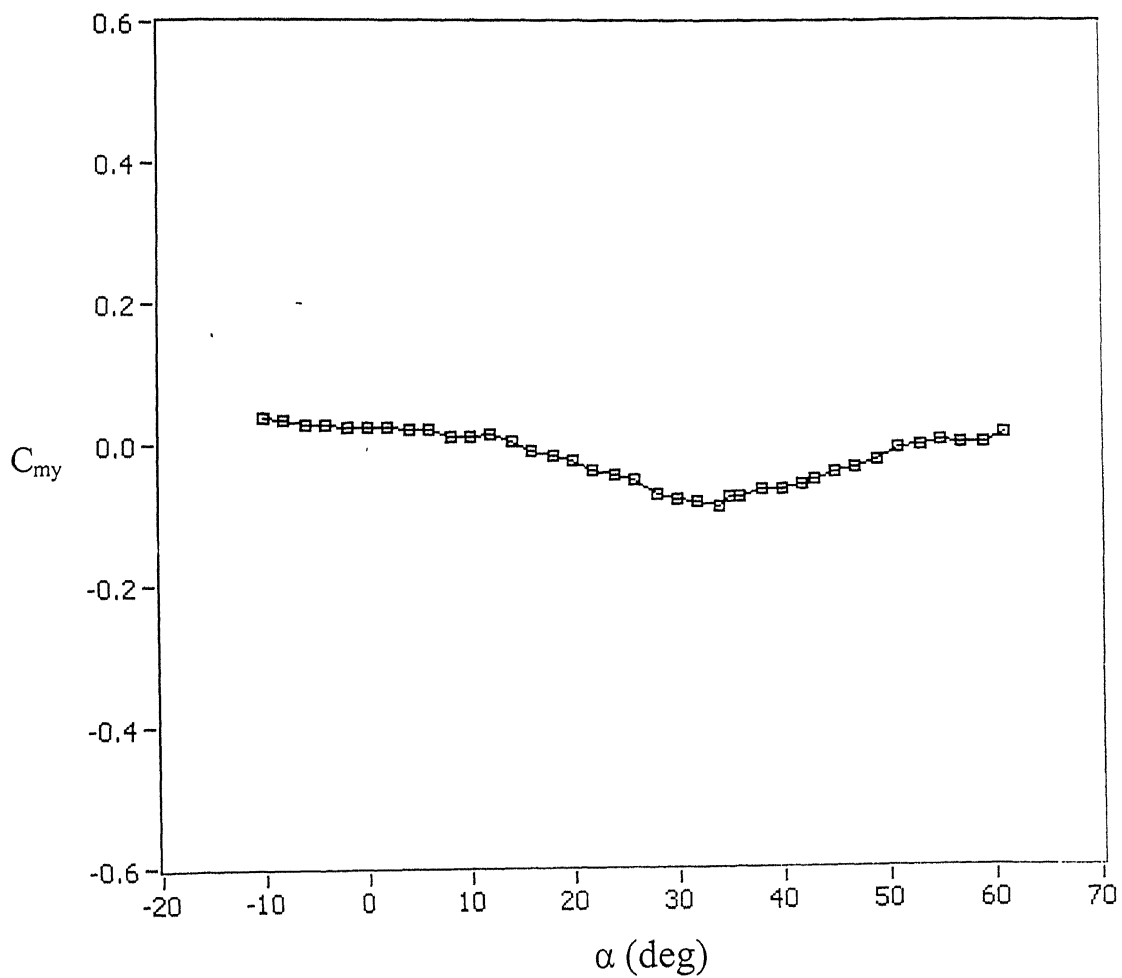


Figure 15: Variation of the yawing moment coefficient ( $C_{my}$ ) with angle of attack at  $\beta = 0^\circ$

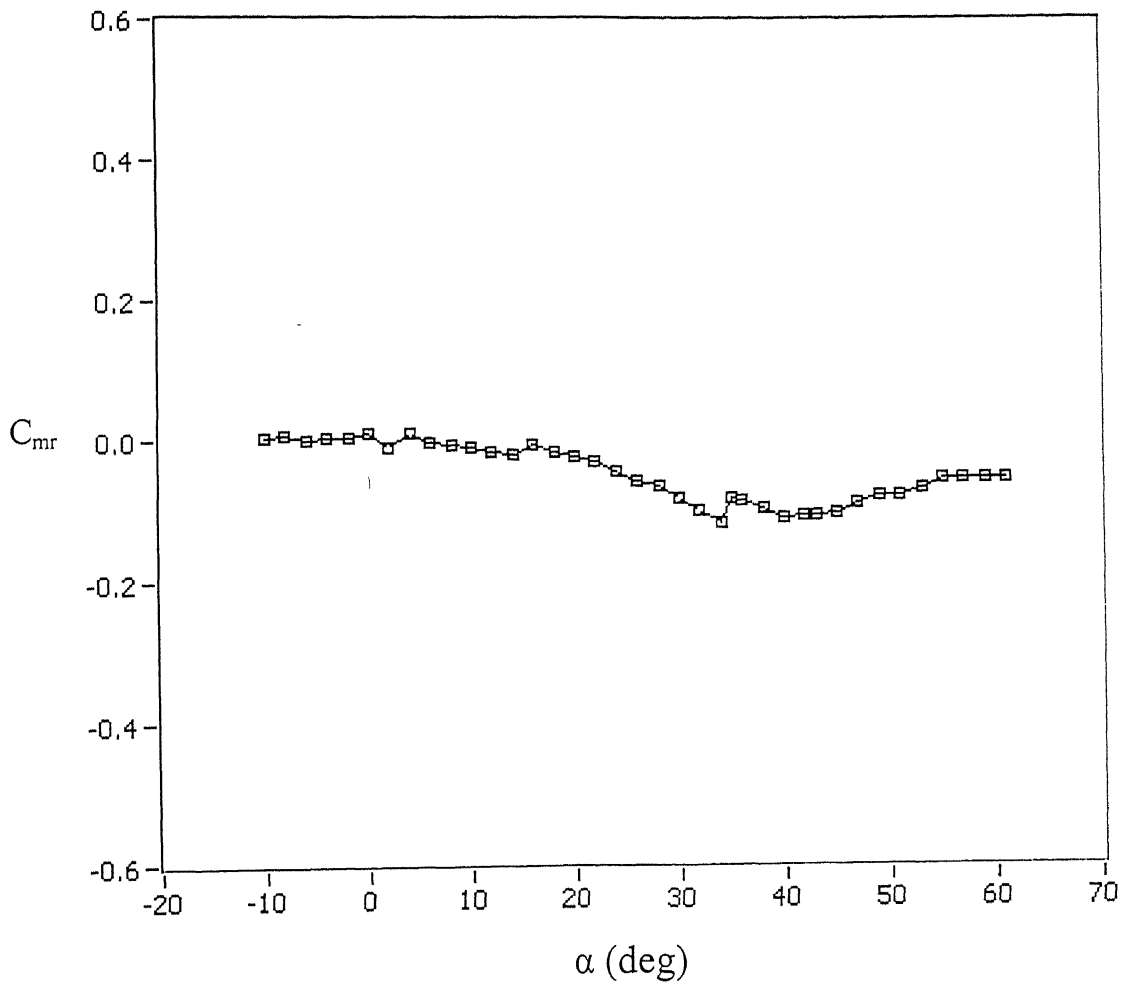


Figure 16: Variation of the rolling moment coefficient ( $C_{mr}$ ) with angle of attack at  $\beta = 0^\circ$



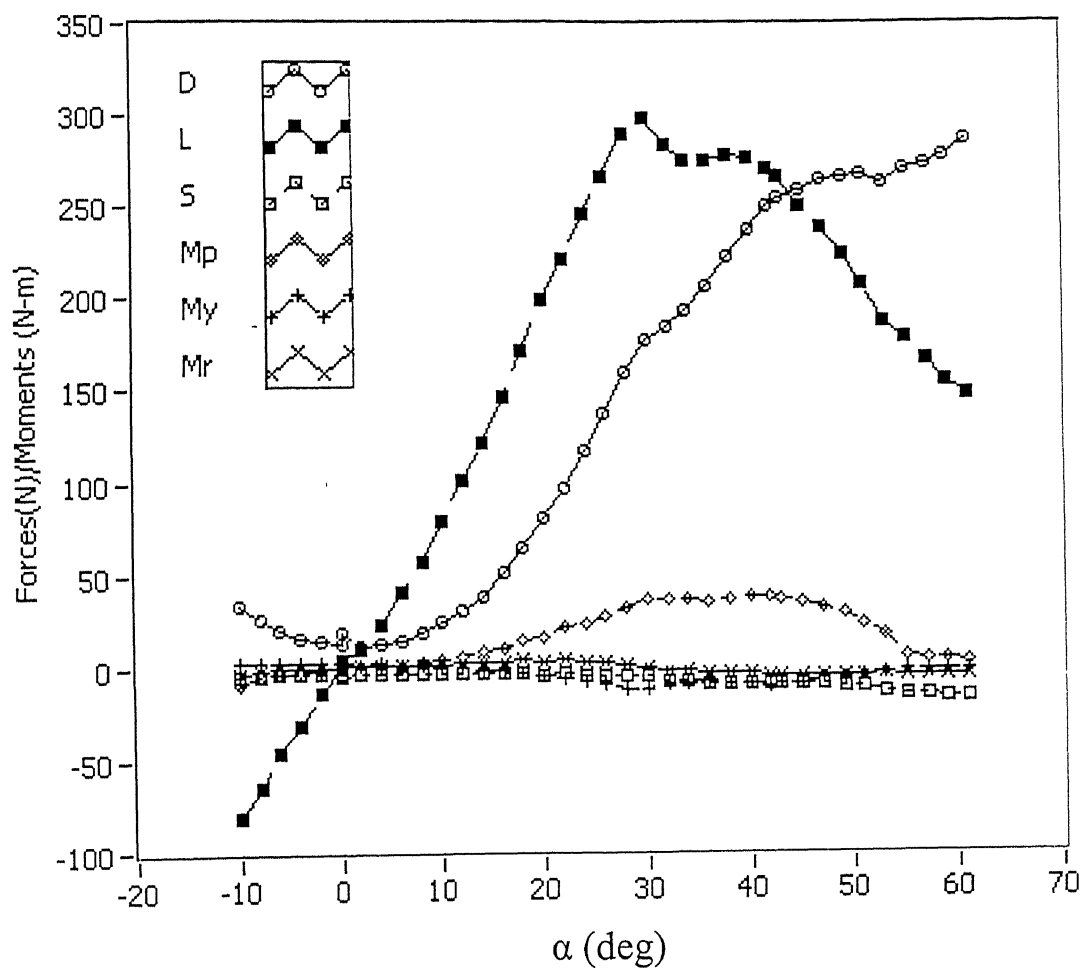


Figure 17: Variation of all aerodynamic forces and moments with angle of attack on wind axis (with  $4.6^\circ$  sideslip angle)

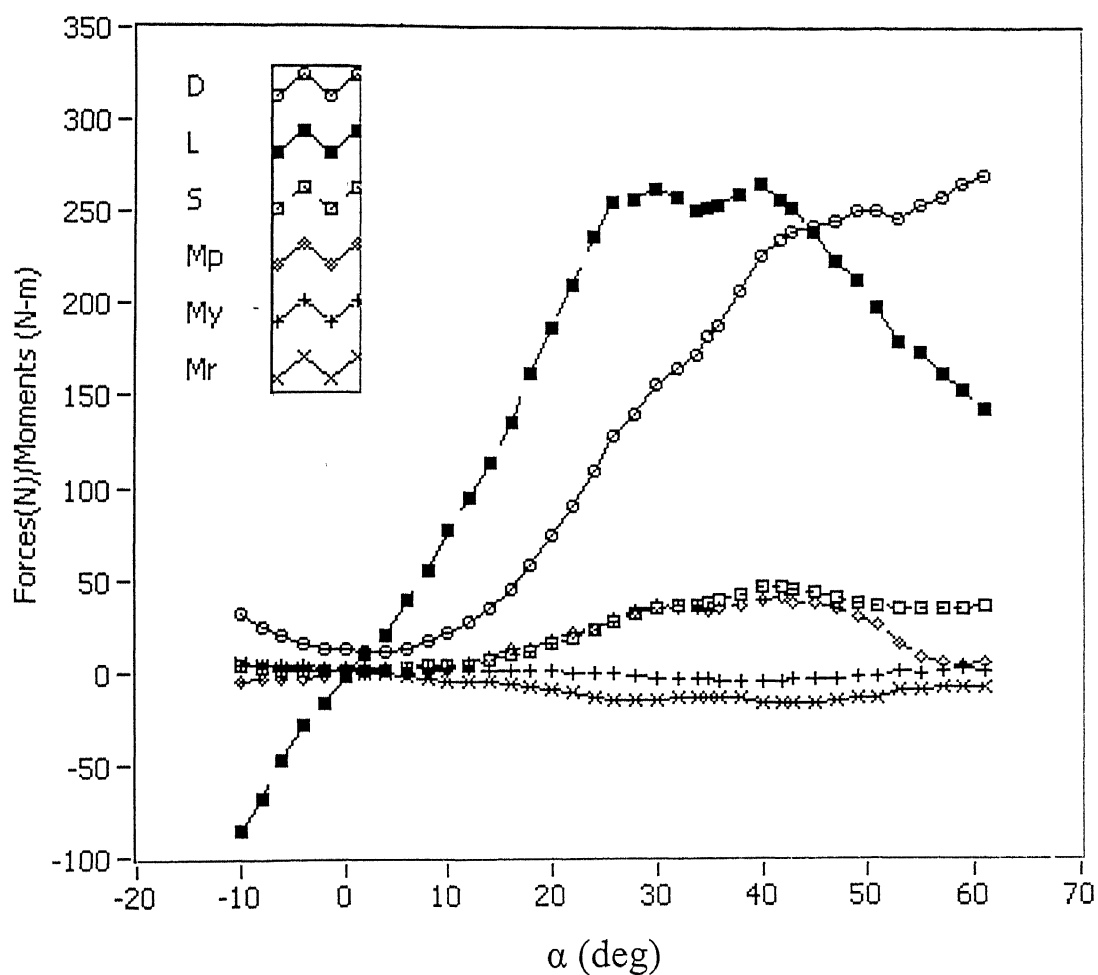


Figure 18: Variation of all aerodynamic forces and moments with angle of attack on wind axis (with  $-5.75^\circ$  sideslip angle)

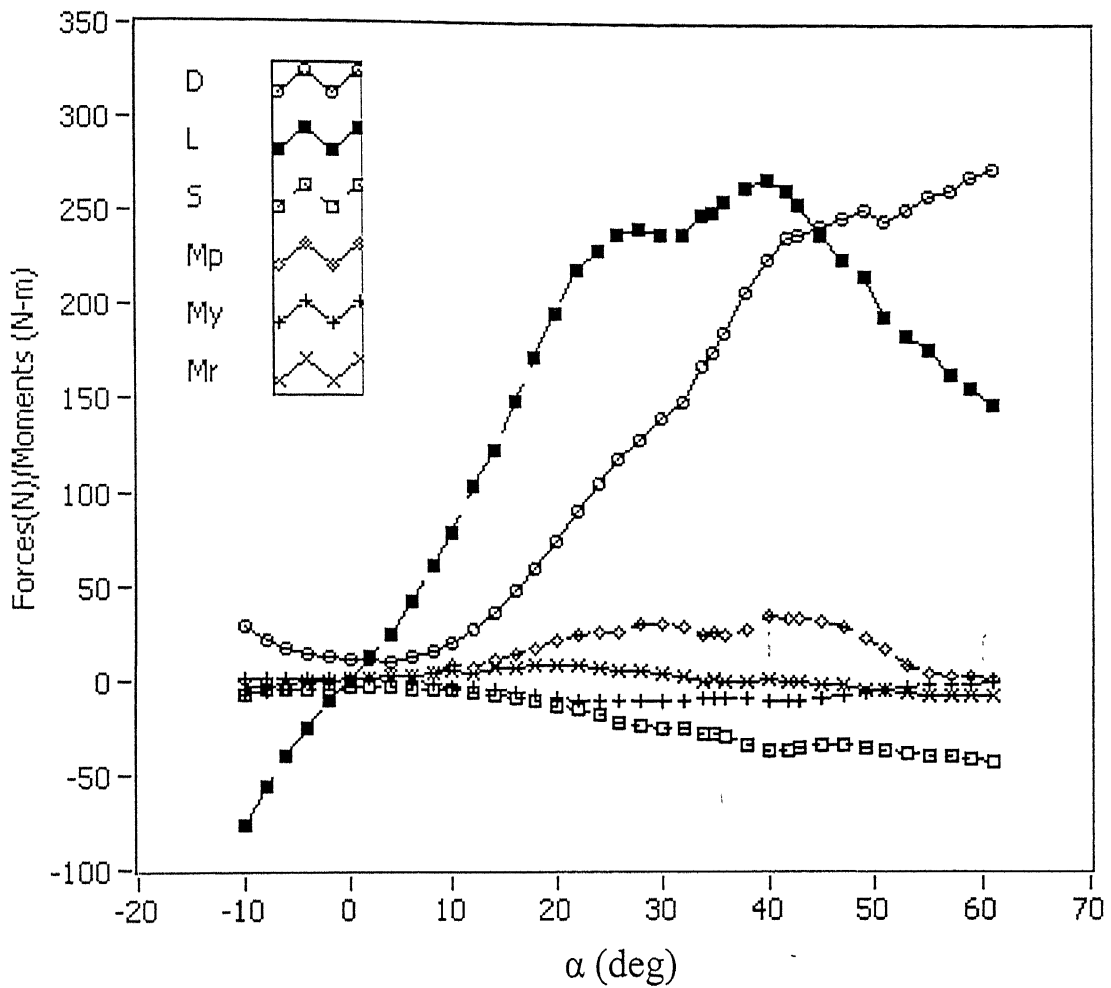


Figure19: Variation of all aerodynamic forces and moments with angle of attack on wind axis (with  $10.12^\circ$  sideslip angle)

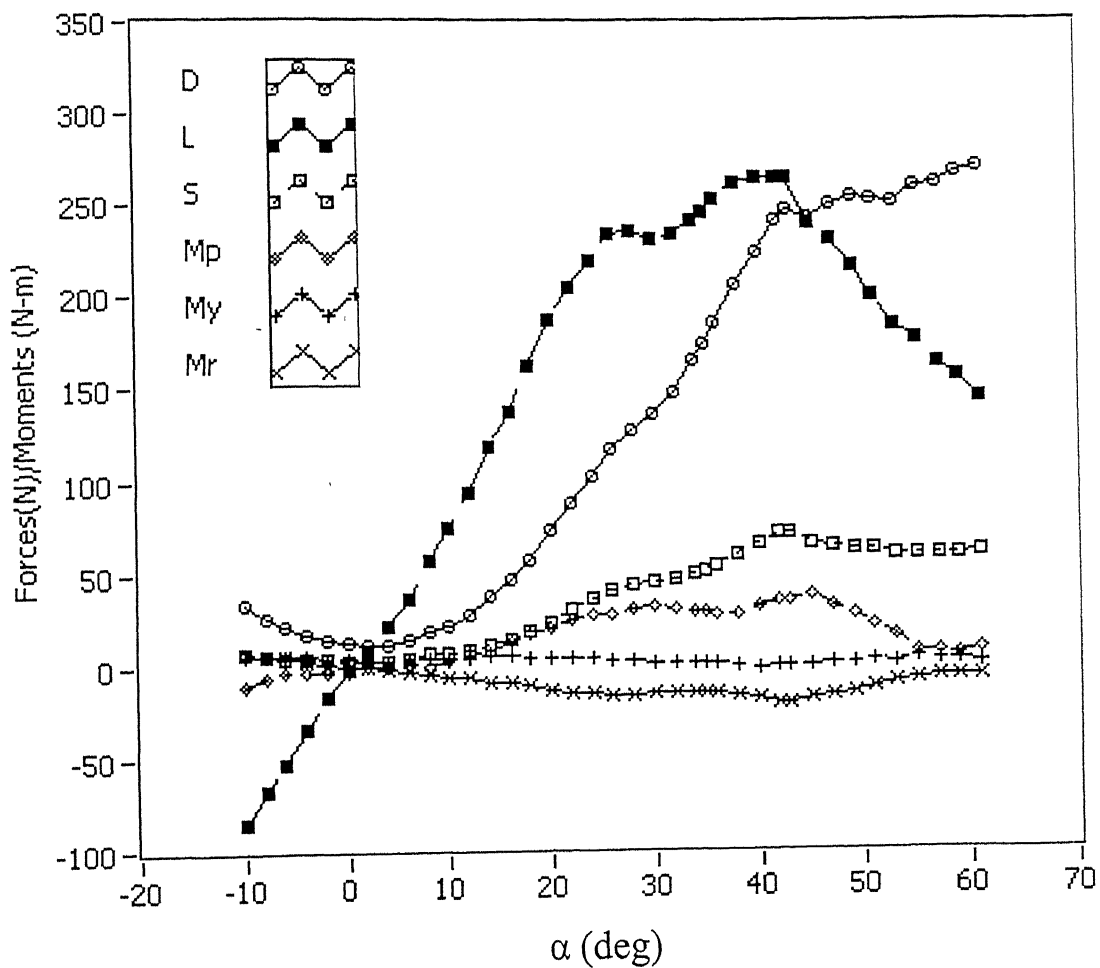


Figure 20: Variation of all aerodynamic forces and moments with angle of attack on wind axis (with  $-10.75^\circ$  sideslip angle)

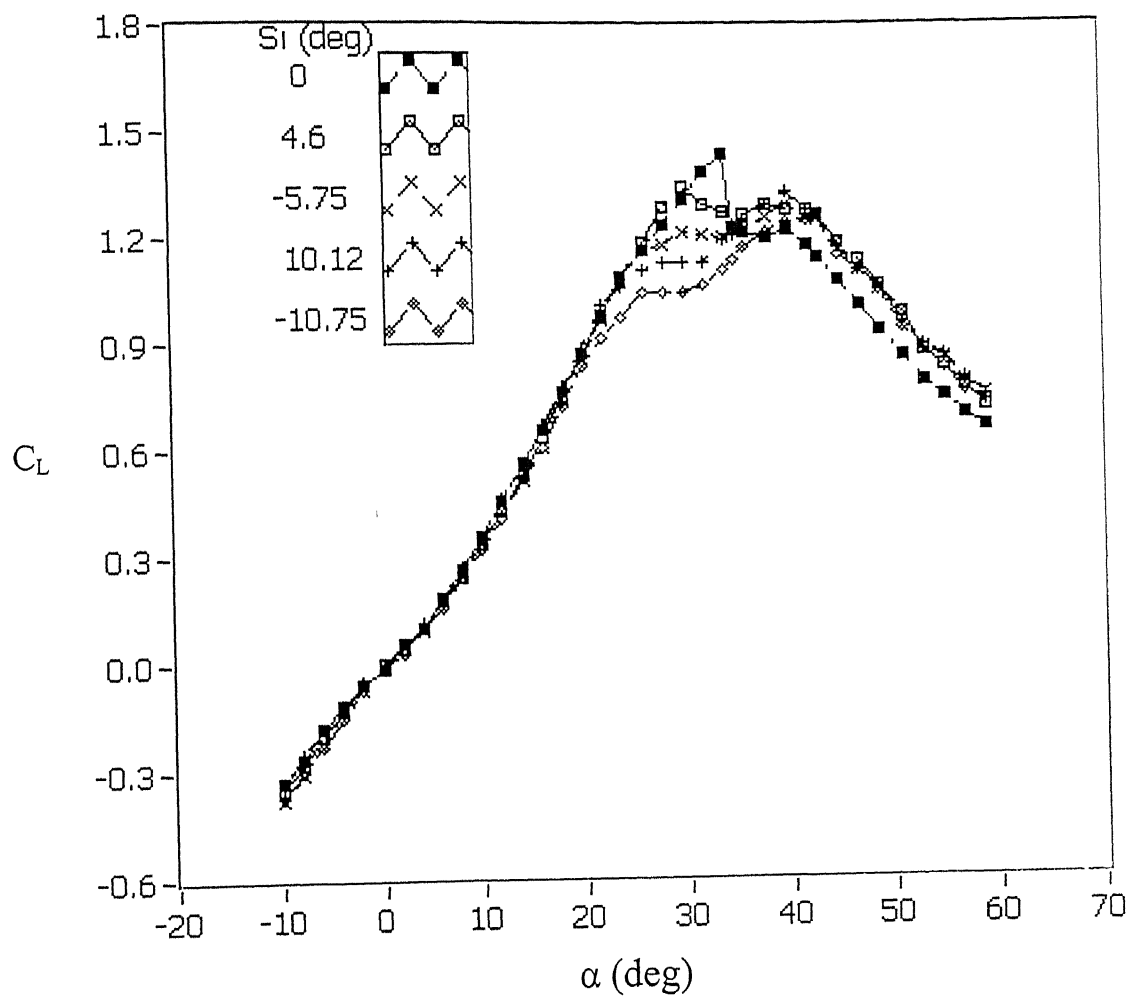


Figure 21: Variation of all lift coefficients with angle of attack (with  $\beta$  as parameter)

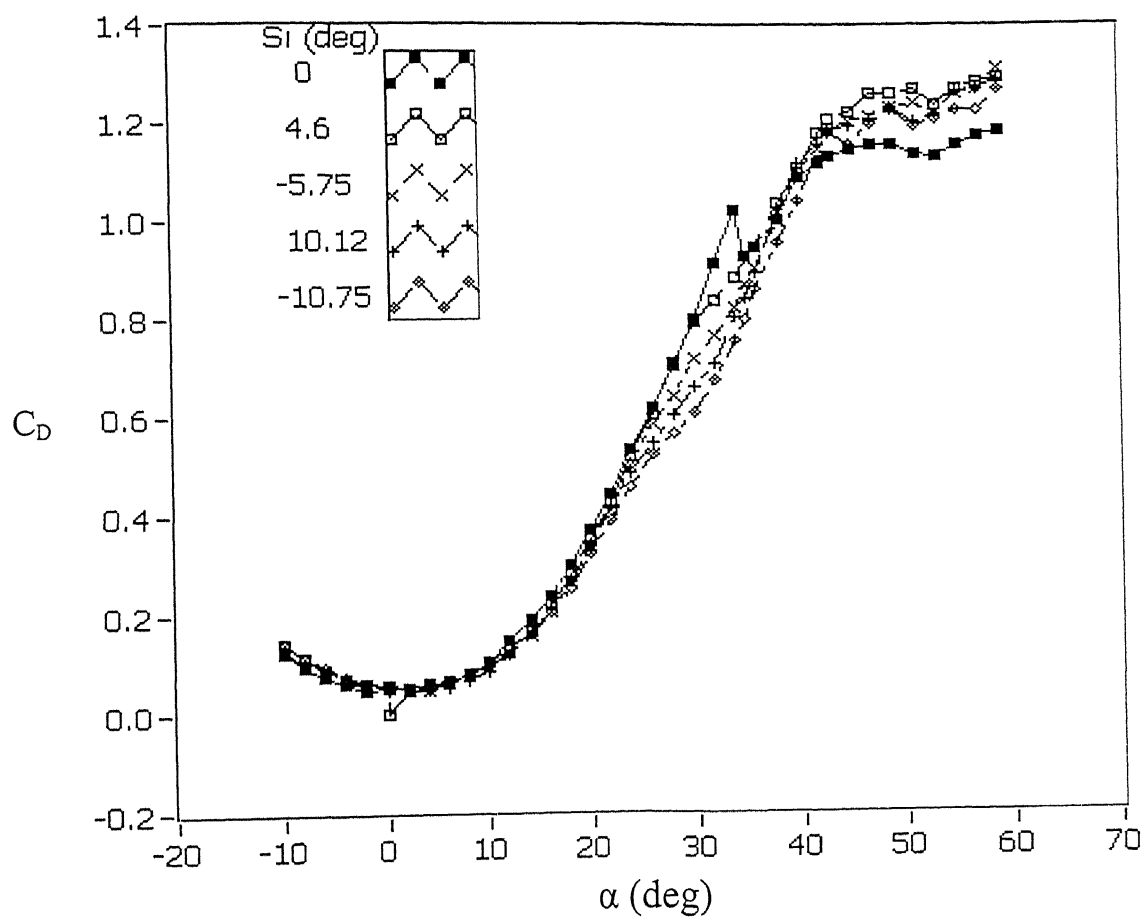


Figure 22: Variation of all drag coefficients with angle of attack (with  $\beta$  as parameter)

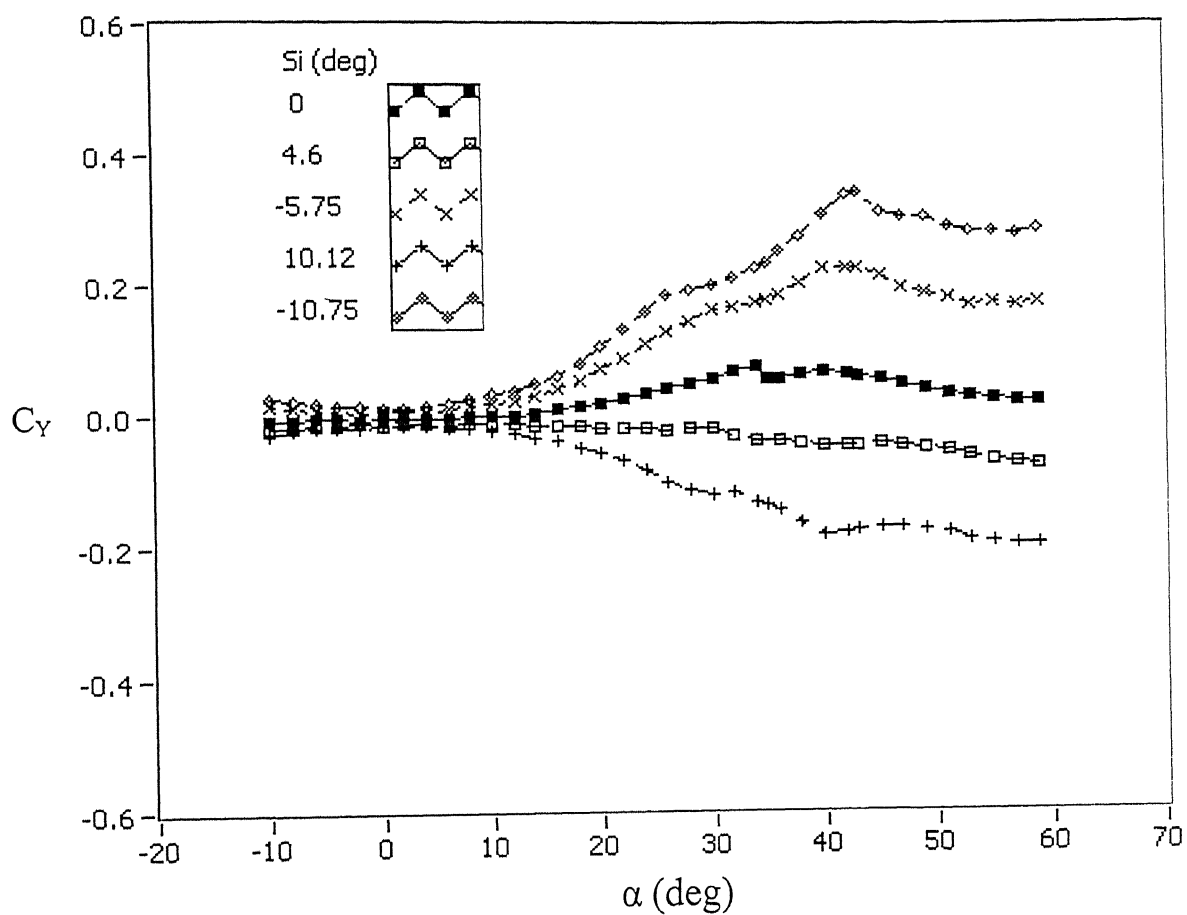


Figure 23: Variation of all side force coefficients with angle of attack (with  $\beta$  as parameter)

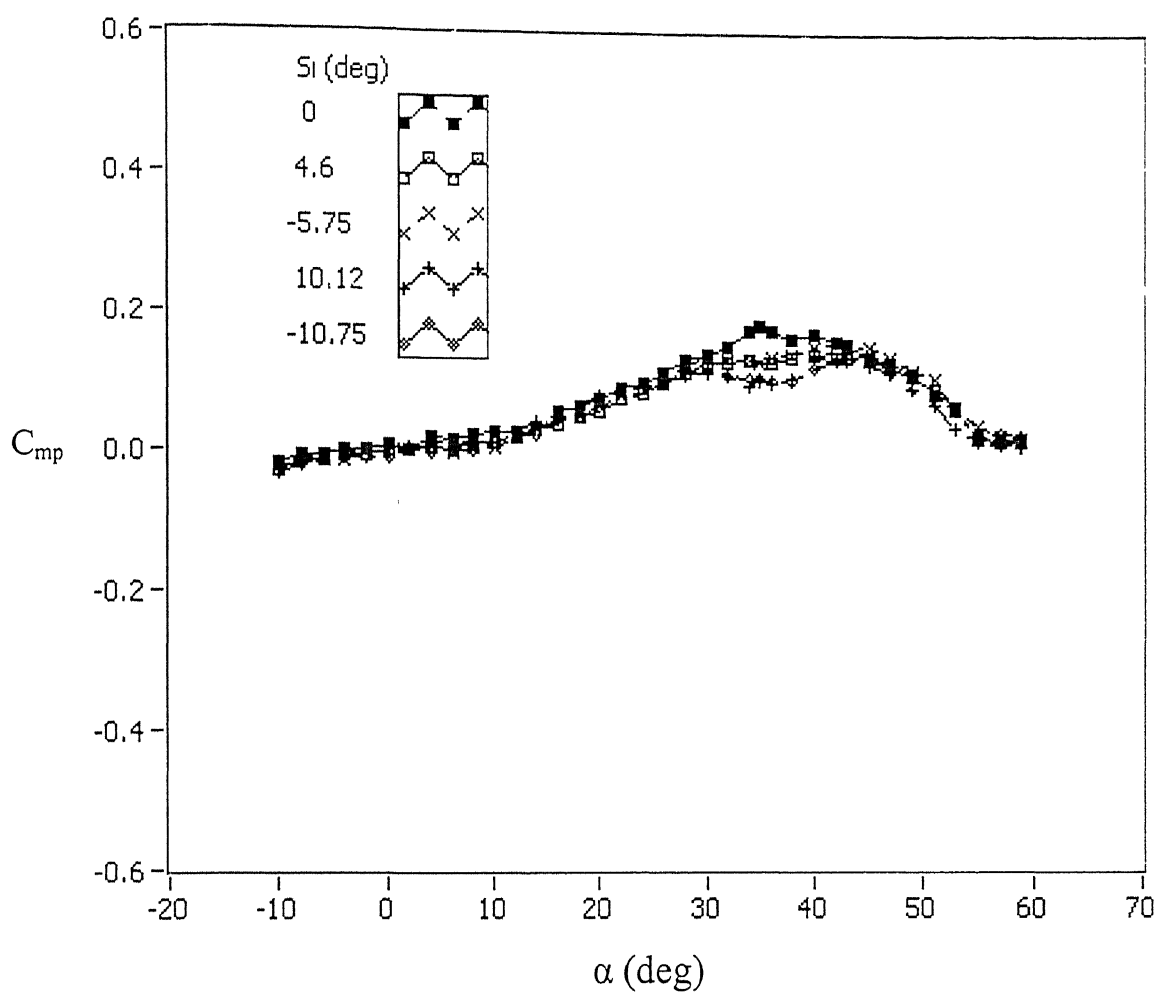


Figure 24: Variation of all pitching moment coefficients with angle of attack (with  $\beta$  as parameter)



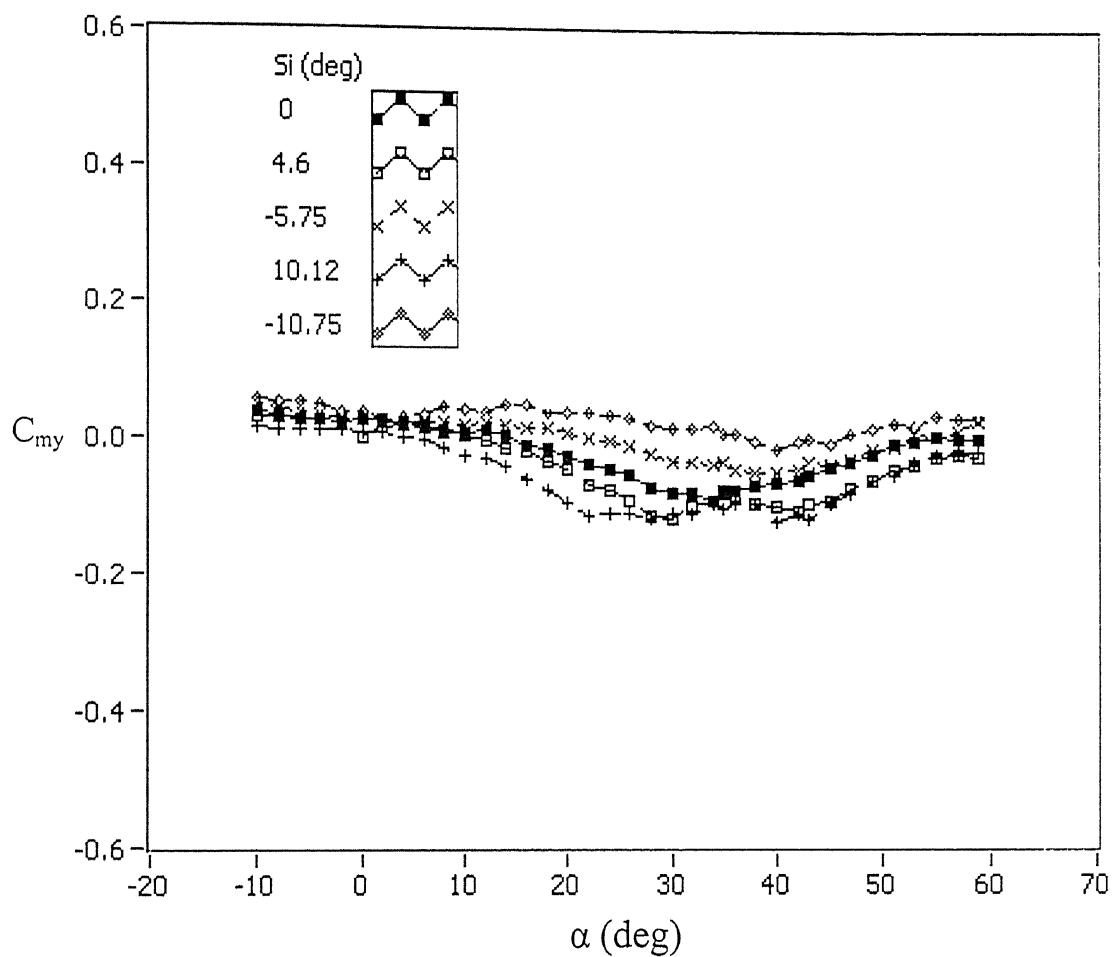


Figure 25: Variation of all yawing moment coefficients with angle of attack (with  $\beta$  as parameter)

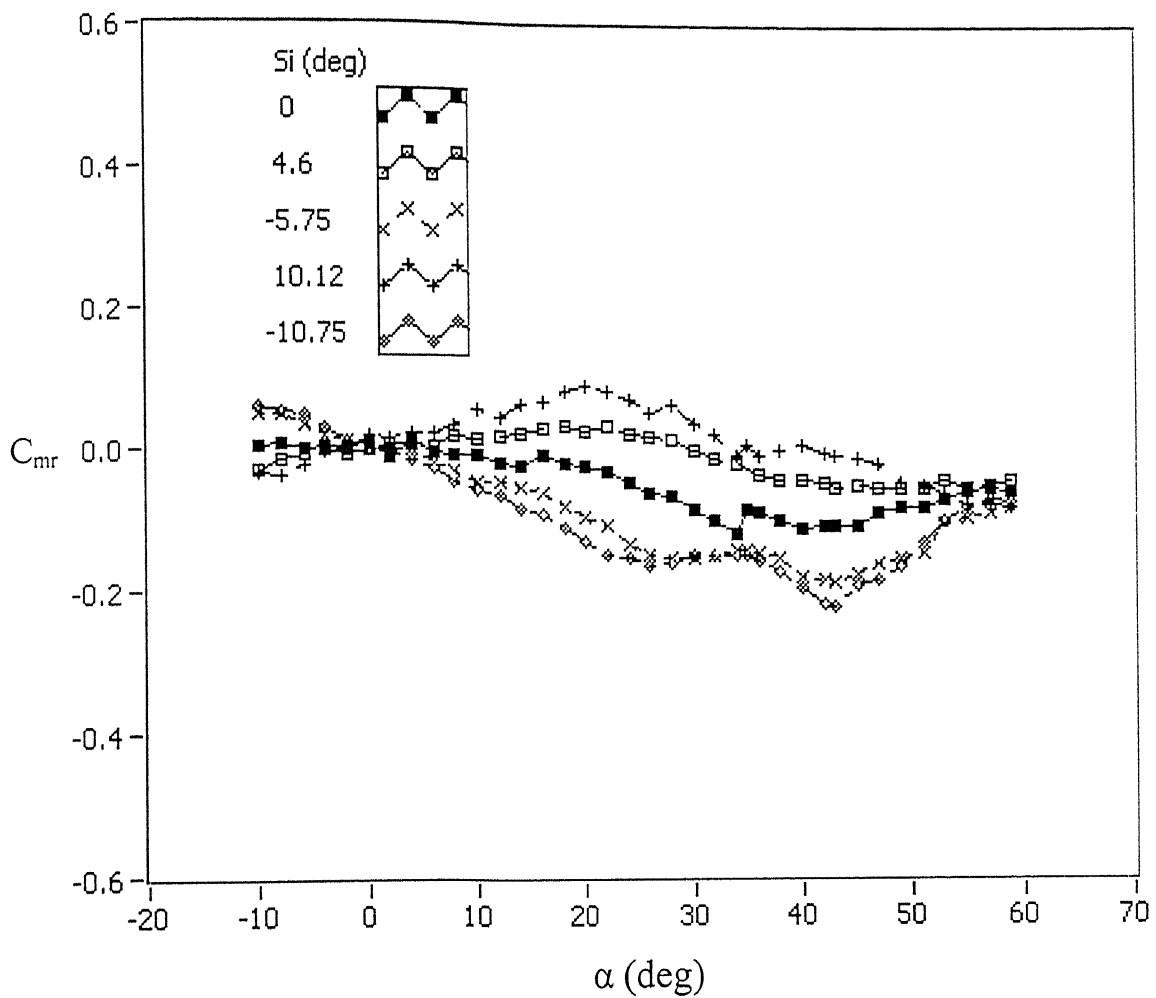


Figure 26: Variation of all rolling moment coefficients with angle of attack (with  $\beta$  as parameter)

पुरुषोत्तम काशीनाथ केवकर पुस्तकालय  
 भारतीय औद्योगिकी संस्थान कातपुर  
 141805  
 अवाप्ति क्र० A

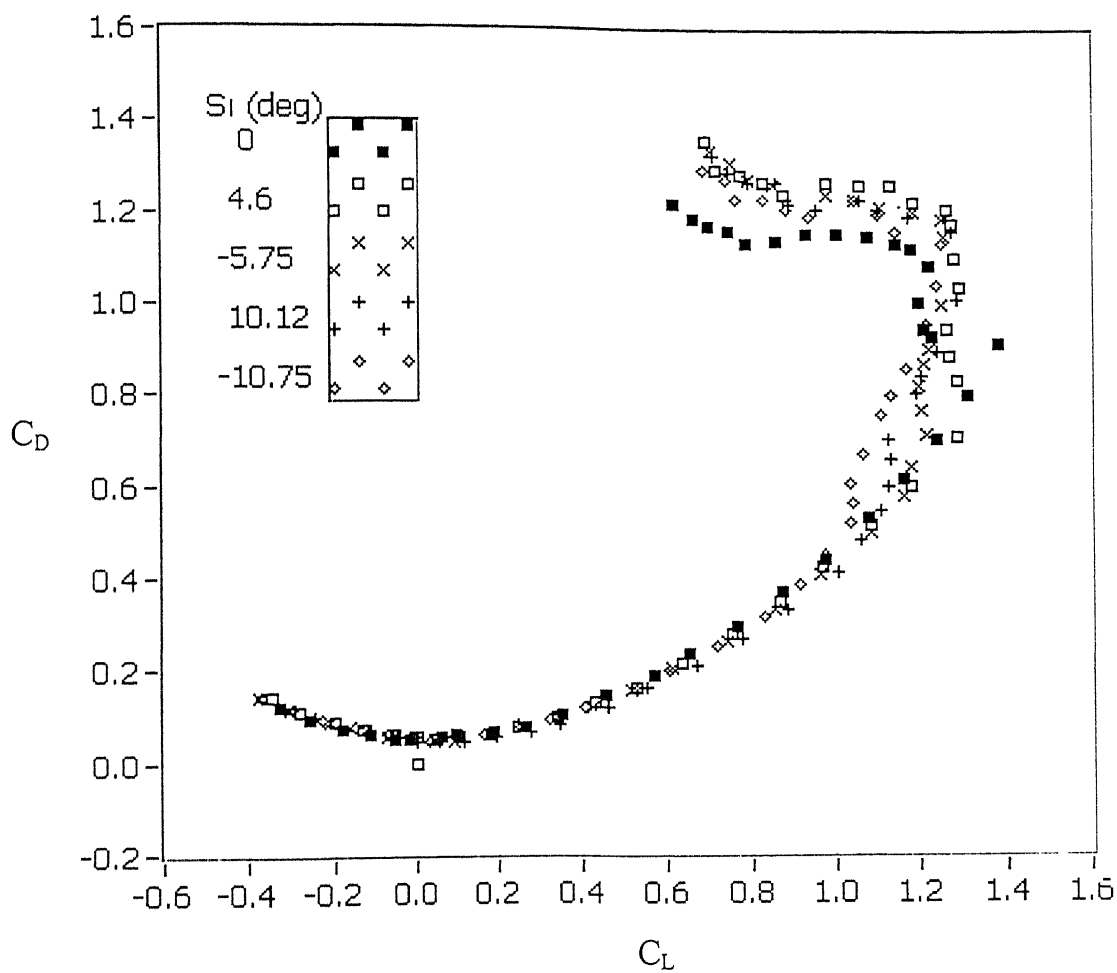


Figure 27 Variation of  $C_D$  with  $C_L$  (with  $\beta$  as parameter)

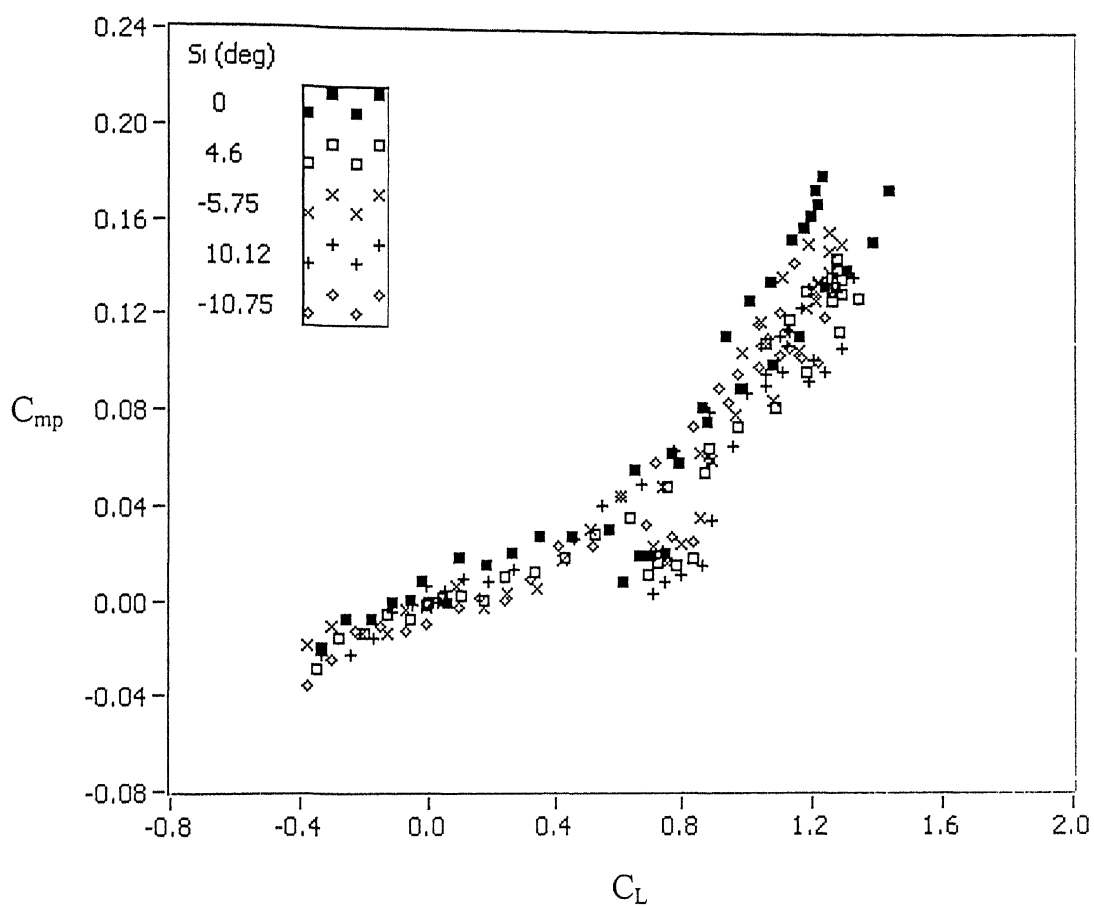


Figure 28: Variation of  $C_{mp}$  with  $C_L$  (with  $\beta$  as parameter)

## APPENDIX-A

A six-component balance is used to measure three forces and three moments in the balance axis coordinate system. The balance comprises of flexible beam elements curved inside a cylindrical body. The forces acting on different planes create tension and compression at desired locations inside the balance body. Strain gages are fixed inside the balance body in a manner to produce electrical output in mille-volt range. The balance needs to be calibrated before it is used to conduct the force measurement experiments.

### *Balances at NWTF*

Balance is fabricated out of Alloy Steel (EN-24). The normal force and side force measuring gages are fixed symmetrical to the center of the balance at a distance of 0.065m. There are two axial force-measuring elements placed on either side of balance center point. All the bridges are configured as summing circuits. Summing circuit requires two gages, which come under tension, placed on one side of the beam and two, which come under compression, on the other side. These internal strain gage balances are used in wind tunnel tests to measure aerodynamic forces and moments acting on a model. Strain gage balances provide output signals in mV range, which are functions of the loads experienced by the balance. The two balances available at NWTF have the following load specifications.

	A	B
Axial force	25 Kg	150 Kg
Side force	35 Kg	150 Kg
Normal force	120 Kg	600 Kg
Rolling moment	13 Kg-m	120 Kg-m
Pitching moment	20 Kg-m	150 Kg-m
Yawing moment	10 Kg-m	120 Kg-m

All forces and moments are specified with reference to balance center.

## ***Balance Calibration***

A six-component balance is typically used to determine the three orthogonal force components and the three orthogonal moment components experienced by the model. It is necessary to calibrate the balance by using a properly designed calibration rig, periodically or prior to the experiment, in order to establish the relation between the loads experienced by the model and signals generated by the strain gages. It is also necessary to have reliable analysis software in order to convert the calibration experiment data into polynomial, usually linear, algebraic equations to determine forces and moments from balance signals. Balance outputs are function of applied loads. In all the conventional calibration methods a calibration formulation of the following form

$$\text{Signals} = \text{Function}(\text{Loads})$$

is valuated. For the use of the balance in the wind tunnel a formulation of the type

$$\text{Loads} = \text{Function}(\text{Signals})$$

is required and this formulation gets simplified using matrix formulation.

During calibration balance is mounted on a calibration rig and standard loads, at predetermined locations on the balance and in predetermined directions, are applied on the balance. The signals from the balance are recorded. Experiments are repeated over a range of load values at each balance location and direction.

### ***Calibration rig***

The calibration rig used is conventional. To calibrate the balance accordingly the balance is connected to the calibration rig with its sting end and a stiff loading sleeve is connected to the model end of the balance. Loads are generated by hanging dead weights attached to the loading sleeve at an appropriate distance from the axis. Lateral loads (side force, yawing moment) are applied after turning the balance through  $90^\circ$  around its rolling moment axis.

### ***Calibration procedure***

In order to load the balance accurately during calibration, it is necessary to have a calibration body, which will transmit the loads to the balance in the same manner as the model would transmit the loads during the tunnel run.

Balance is mounted in horizontal direction using an adapter fitted within frame over the calibration rig. A calibration body is used for load application. This body slides on the balance and load transfer takes place over tapered balance front end area. Direct loads N1, N2, S1 and S2 are applied at required points directly on this calibration frame using a loading frame. For this purpose, loading frame has pointed fulcrum points at one end and load application pan at the other end. Rolling moment is applied using a bar on top of the loading frame and two loading pans are used for rolling moment application. Equal weights are put on left hand side and right hand side pans and weight shifting from left pan to right pan creates positive rolling moment. For axial force loading, a pulley is attached at the front face of the calibration frame and axial force load is applied using gravity loading.

A data acquisition program written in LabVIEW software is used to acquire all 6 balance channels along with the balance excitation voltages. The balance output is normalized to excitation voltage. Thus, we have mV/V level balance output. Various single component loadings are performed and respective data sets comprising of the applied load and normalized output is stored in the balance raw data file for calculating the error in work back loads (i.e. actual load minus predicted load) and the results are plotted w.r.t. number of samples for respective loadings. Experiments are conducted over arrange of load values at each balance location and direction.

### *Analysis method*

Analysis of data from the calibration is a necessary step before the balance can be used. Here slope method is used.

#### *Slope method*

In this method, for each data set the six signals obtained from the balance are plotted against the applied load and straight line fits are obtained. For example, if the load applied in N1 component, then each of the six signal components  $a_x$ ,  $n1$ ,  $n2$ ,  $s1$ ,  $s2$ , and  $R_m$  are plotted against the applied load N1, and the six straight line fits are obtained by least square technique. This procedure is repeated for six data sets to obtain 36 coefficients,  $C_{ij}$ , as shown in the following equation.

$$S_i = \sum_{j=1}^6 C_{ij} L_j$$

These coefficients,  $C_{ij}$ , from the elements of the forward matrix (or coefficient matrix). When the load matrix  $L_i$  (a  $6 \times 1$  column matrix) is pre-multiplied by the  $6 \times 6$  forward matrix, the result is the signal matrix,  $S_i$ . The forward matrix is inverted to obtain the inverse matrix. When the inverse matrix is pre-multiplied to the signal matrix, the load matrix is generated.

$$L_i = \sum_{j=1}^6 C_{ij}^{-1} S_j$$

The predicted loads are at the balance center. These loads are first transformed to the body axes from which it is finally transformed to wind axis system. These transformations are outlined below.

### *First order method*

Here each element of the matrix  $[C]$  is such that

$$L_i = \sum_{j=1}^6 C_{ij} S_j$$

is obtained from the specified set out of the six sets of calibration data. For example all members of the first row are obtained from the slopes of the signals against the applied load  $Ax$ . The elements of the further rows are obtained from the respective loading sets.

### *Second order method*

If the linear fit is considered unsatisfactory, a second order fit (matrix B) can be considered. In this case the matrix will have 6 linear terms and 21 second order terms thus resulting in 27 terms.

$$L_i = \sum_{j=1}^6 A_{ij} S_j + \sum_{j=1}^6 \sum_{k=j}^6 B_{ijk} S_j S_k$$

Linear terms:  $ax, n1, n2, s1, s2, rm$

Second order terms:  $ax \times ax, n1 \times n1, n2 \times n2, s1 \times s1, s2 \times s2, rm \times rm$

$ax \times n1, ax \times n2, ax \times s1, ax \times s2, ax \times rm$

$n1 \times n2, n1 \times s1, n1 \times s2, n1 \times rm$

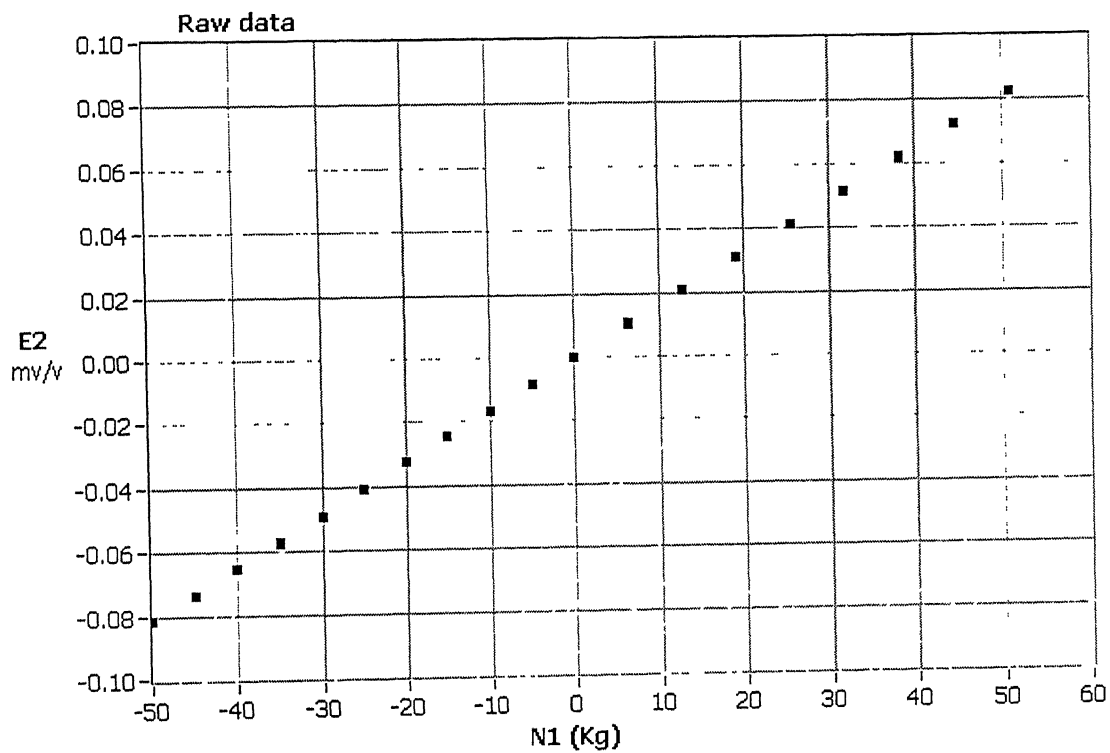
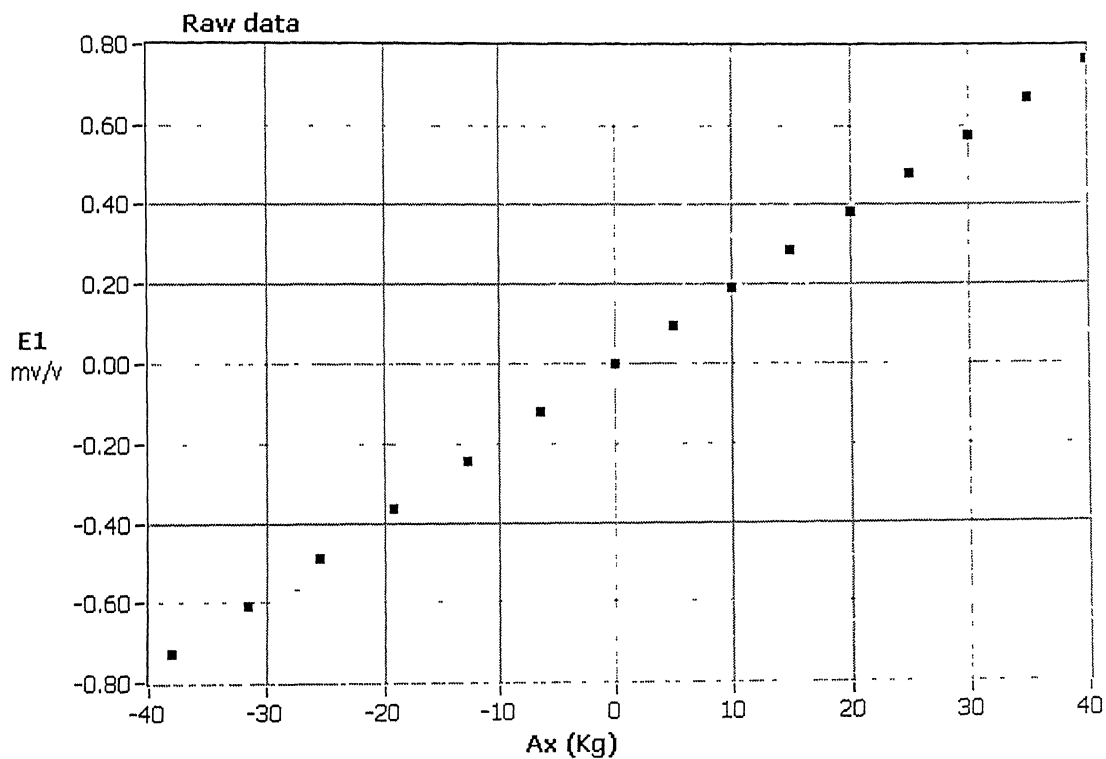
$n2 \times s1, n2 \times s2, n2 \times rm$

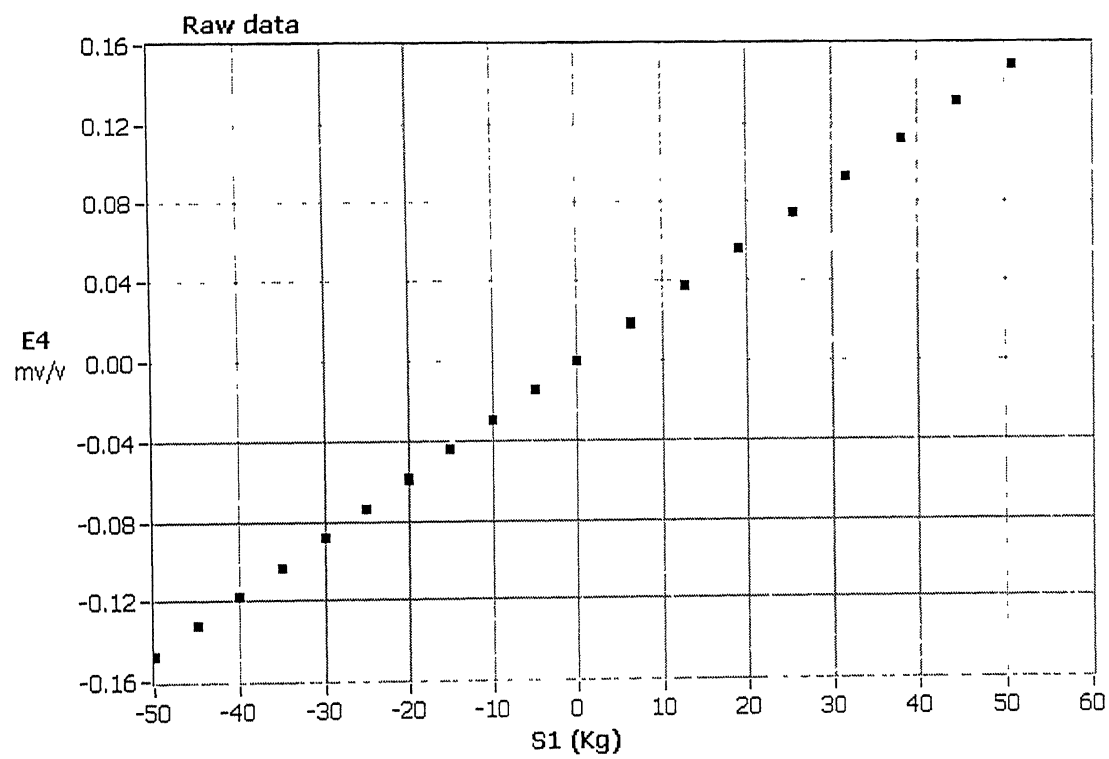
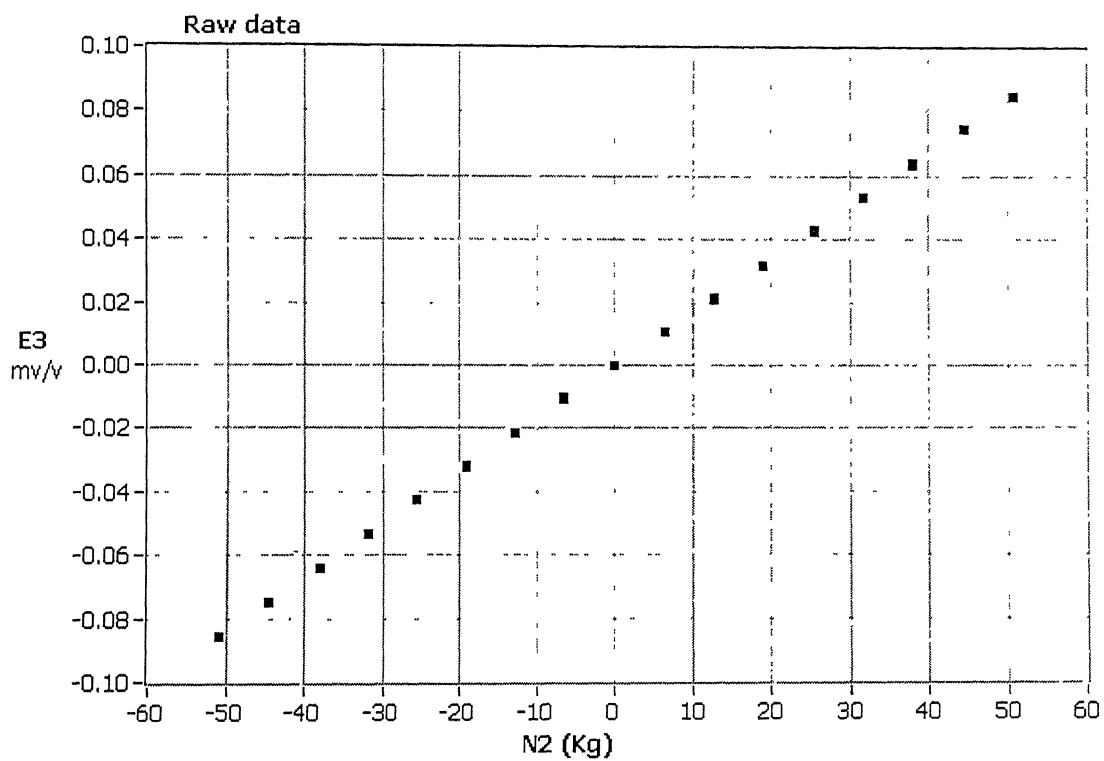
$s1 \times s2, s1 \times rm$

$s2 \times rm$



Calibration curves for balance B (primary loading):





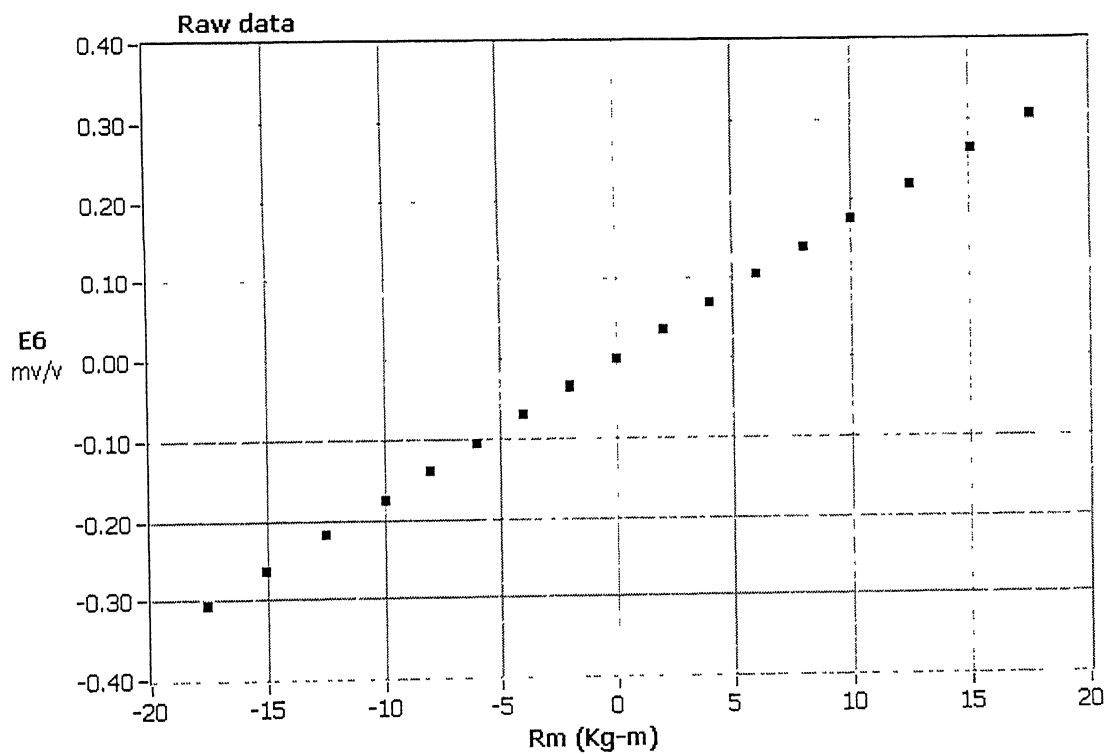
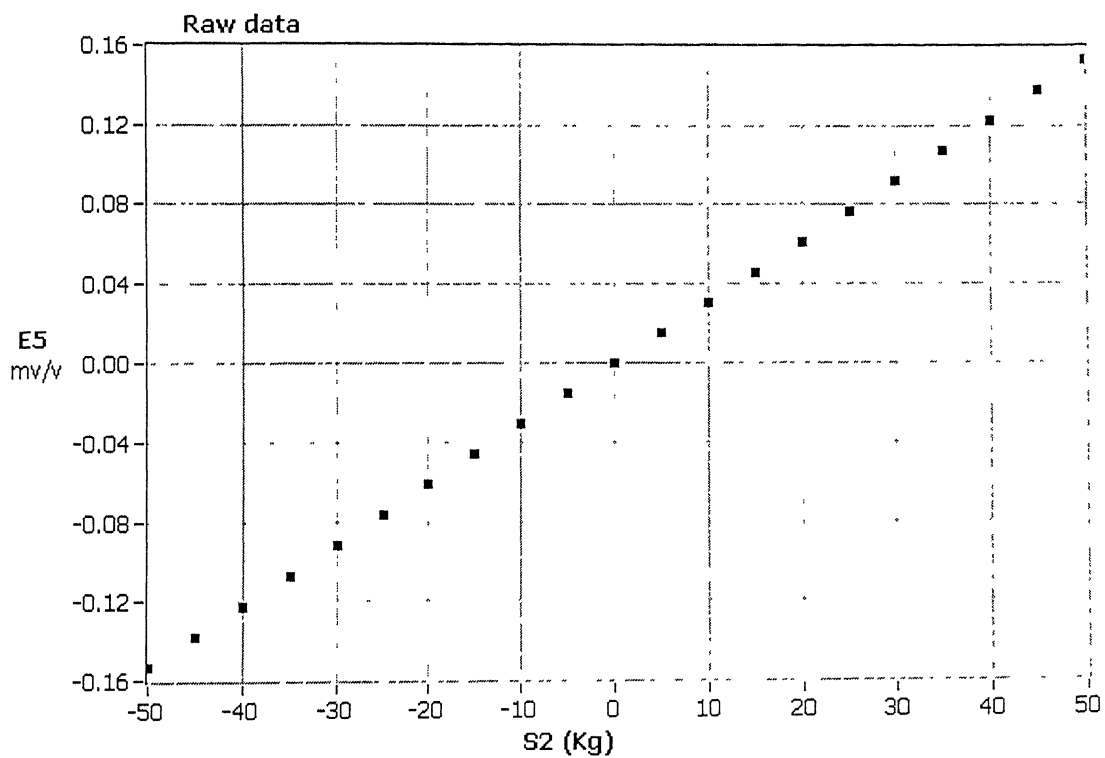


Table 1: Calibration coefficients matrix (Slope method)

52.202731	6.945109	6.577363	1.351733	0.125910	-0.675661
-0.552789	613.018111	12.293371	-8.782353	-0.796523	9.754448
-0.173987	-6.354929	595.023845	0.051371	-16.980937	9.804244
-0.555678	-8.908583	1.761439	339.570628	5.983684	16.887103
0.412637	0.146925	13.584656	-7.428766	325.150796	-10.692676
0.001586	-0.355012	-0.340933	0.050107	0.737577	57.383483